

# Utilizing ink composition to tune bulk-electrode gas transport, performance, and operational robustness for a Fe–N–C catalyst in polymer electrolyte fuel cell

Luigi Osmieri<sup>a,1</sup>, Guanxiong Wang<sup>a,1</sup>, Firat C. Cetinbas<sup>b</sup>, Sunilkumar Khandavalli<sup>a</sup>, Jaehyung Park<sup>b</sup>, Samantha Medina<sup>c</sup>, Scott A. Mauger<sup>a</sup>, Michael Ulsh<sup>a</sup>, Svitlana Pylypenko<sup>c</sup>, Deborah J. Myers<sup>b</sup>, K.C. Neyerlin<sup>a,\*</sup>

<sup>a</sup> National Renewable Energy Laboratory, Golden, CO, USA

<sup>b</sup> Argonne National Laboratory, Lemont, IL, USA

<sup>c</sup> Department of Chemistry, Colorado School of Mines, Golden, CO, USA

## ARTICLE INFO

### Keywords:

PGM-Free catalyst  
Mass transport resistance  
Ionic resistance  
Ionomer distribution  
Nano-CT  
Ink composition

## ABSTRACT

With lower site density and turnover frequency, platinum group metal (PGM)-free catalysts based electrodes are often greater than 50  $\mu\text{m}$  thick in order to increase performance across the fuel cell operating range. Consequently, PGM-free electrodes have an additional bulk electrode transport resistance beyond the local or aggregate level transport in thin platinum-based electrodes. In parallel to the development of more active and durable PGM-free catalysts, advancements in understanding the interplay between PGM-free electrode fabrication, bulk-electrode transport, proton conductivity and performance are needed. Here, the relationship between ionic and gas phase transport through the electrode thickness is modified by adjusting electrocatalyst and ionomer flocculation/interaction at the ink level. The influence of the ink composition (water/n-propanol content) is examined via various in-situ electrochemical and ex-situ characterization techniques and the resulting electrode structure/performance relationship contrasted with electrode performance robustness across a range of relative humidity (RH). For the electrocatalyst examined here, a water-rich (82 wt%  $\text{H}_2\text{O}$ ) ink formulation was favorable for operation at high RH due to improved molecular diffusion through larger electrode pores. In contrast, the improved interactions between ionomer and electrocatalyst enabled a more robust electrode and higher performance during low RH operation for the 50 wt%  $\text{H}_2\text{O}$  content ink.

## 1. Introduction

An ever increasing amount of the world's energy is originating from renewable sources [1,2]. Due to the intermittent character of the renewable sources, energy storage is essential, and the production of  $\text{H}_2$  via  $\text{H}_2\text{O}$  electrolysis is a promising solution [3,4]. In this view,  $\text{H}_2$  will be used as an energy vector, and its utilization as fuel in polymer electrolyte fuel cell (PEFC) devices for stationary and transportation applications is essential [5,6].

While Pt is the best catalyst for both the electrochemical reactions occurring in an acidic PEFC, hydrogen oxidation reaction (HOR) and oxygen reduction reaction (ORR) [7,8], it is both costly and scarce, with the potential to suffer supply problems and unsustainable cost increase

in a scenario of considerably higher demand for PEFC manufacturing [9, 10]. Due to the more sluggish ORR kinetics, most of the Pt is placed on the cathode of a PEFC [11,12]. For this reason, intense research efforts have been done in the last decades in the field of platinum group metal (PGM)-free catalysts for ORR, to improve the activity and durability of these catalytic materials. Among different types of PGM-free catalysts for ORR, the most promising are carbon-based materials containing N and Fe (often indicated as Fe–N–C catalysts) [13–18]. These research efforts have recently led to the commercialization of the first PEFC portable device using a PGM-free catalyst [19]. However, the more demanding power density requirements of automotive PEFCs mean that they still rely heavily on Pt-based electrocatalysts [20]. Thus, further research is needed to improve PGM-free based PEFC to make them

\* Corresponding author.

E-mail address: [kenneth.neyerlin@nrel.gov](mailto:kenneth.neyerlin@nrel.gov) (K.C. Neyerlin).

<sup>1</sup> These authors contributed equally in the work.

suitable for transportation applications.

Despite the lower cost and improved tolerance to contaminants [19], the lower volumetric activity of PGM-free catalysts means higher loadings, and correspondingly thicker electrodes are needed to achieve reasonable electrode performances. Consequently, a typical PGM-free cathode catalyst layer (CCL) can be 5–10 times thicker than a standard Pt/C CCL [12,21], resulting in higher mass transport and  $H^+$  resistances in the CCL, thereby limiting high current density performance [21–24].

As recently pointed out in the literature, challenging limitations exist in increasing the intrinsic activity of PGM-free catalysts in terms of turnover frequency and active sites density [19,25]. Additionally, from a stack perspective, one cannot simply add more cells without significantly increasing the cost of all stack components, offsetting any financial motivation for investigating PGM-free electrocatalysts [26]. For these reasons, the thickness of PGM-free CCLs will likely remain high in the near term, requiring major improvements in electrode mass transport and  $H^+$  conductivity for PGM-free electrodes [19,25]. These properties are influenced by several variables, with catalyst loading and ionomer content the most clearly identifiable [23,27–29]. Many other parameters also play a critical role, such as; i) ionomer chemistry [24, 30], ii) ink composition, concentration and processing [31–33], iii) electrode fabrication method [34–36], and iv) drying conditions [28] to name a few. Further complicating matters, the changing chemistry and morphology of each novel electrocatalyst may require its own electrode fabrication optimization.

A systematic investigation of these variable on CCL features and PEFC performance has not been carried out thus far for PGM-free electrodes, most likely because most research has focused primarily on the development of innovative PGM-free catalysts materials, to meet activity and durability targets when compared to Pt-based catalysts benchmarks. However, due to the increased thickness, the effects of mass transport and ionic conductivity in PGM-free PEFCs electrodes are more impactful than in PGM electrodes. Thus, focusing on CCL development and optimization is a critical research direction in parallel with catalyst development [19,25,37].

In this work, it is demonstrated how a simple electrode fabrication parameter, namely the water and alcohol relative contents in water/alcohol (n-propanol) based inks, plays a crucial role in enhancing the PEFC performance of a PGM-free catalyst. The PGM-free catalyst used was a commercial Fe–N–C material from Pajarito Powder, LLC. The observed performance differences are discussed in terms of how ink water content affects  $H^+$  conductivity and bulk-electrode gas phase mass transport. PGM-free CCL properties are quantified at the membrane electrode assembly (MEA) level using *in-situ* electrochemical diagnostics: cyclic voltammetry (CV), electrochemical impedance spectroscopy (EIS), and HOR limiting current to obtain information about the ionomer-catalyst interface [38,39],  $H^+$  resistance of the CCL [40–43], and bulk-electrode gas transport resistance in the CCL, respectively [27,44]. The values of bulk-electrode gas transport resistance are contrasted with those limiting high current density performance for low PGM electrodes and discussed relative to other cell level resistances for PGM-free systems.

The results from the electrochemical diagnostics are supported with characterization of the resulting electrode morphology through scanning transmission electron microscopy (STEM) micrographs combined with energy dispersive spectroscopy (EDS) of MEA cross sections, along with nano-scale resolution X-ray computed tomography (nano-CT), illustrating the ability to tune electrode transport properties by impacting catalyst/ionomer interactions and aggregation by changing the water content of the catalyst ink. Overall, up to a 50% performance improvement is observed for  $H_2$ /air polarization measurements at high current density, demonstrating that electrode optimization balancing proton conductivity and bulk-electrode gas transport may be as crucial as the development of new PGM-free electrocatalysts.

## 2. Experimental

### 2.1. MEA fabrication

The cathode catalyst ink was prepared by mixing 30 mg of a PGM-free Fe–N–C catalyst (PMF-011904, Pajarito Powder LLC, Albuquerque NM, USA) with 0.347 mL of a 5 wt% Nafion ionomer solution with equivalent weight (EW) = 1100 (LIQUION LQ-1105, Ion Power Inc.) and variable amounts of n-propanol (nPA, Sigma Aldrich) and deionized (DI)  $H_2O$  (Ultrapure Millipore > 18 M $\Omega$ ) according to the desired  $H_2O$  content in the ink. The wt%  $H_2O$  content in the ink is defined as follows:  $100 \cdot m_{H_2O} / (m_{H_2O} + m_{nPA})$ , where m indicates the mass. The total volume of DI  $H_2O$  + nPA was kept constant. With this formulation the dry Nafion ionomer content in the electrode was ca. 35 wt%, and the ink concentration was kept constant to 26 mg of catalyst per mL of liquid. The ink was sonicated in an iced bath for 3 h.

The anode catalyst ink was prepared by mixing 160 mg of a Pt/C catalyst (50 wt% Pt on high surface area carbon catalyst TEC10E50E, TKK Corp., Japan) with 0.338 mL of a 20 wt% Nafion ionomer solution with EW = 1000 (D2020, Ion Power Inc.), 21 mL of DI  $H_2O$ , and 16 mL of nPA. With this formulation the ionomer-to-carbon (I/C) ratio on the anode catalyst was ca. 0.86. The ink was sonicated first with a horn sonicator for 20 s and then placed in an iced bath sonicator for additional 20 min. Then the ink was ultrasonically spray coated onto a carbon paper gas diffusion layer (GDL) with microporous layer (Sigracet 29BC, SGL Carbon) with a loading of  $0.2 \text{ mg}_{Pt} \text{ cm}^{-2}$  to form a gas diffusion electrode (GDE). The ultrasonic spray coating system used was a Sono-Tek Exacta Coat model, with a 25 kHz accumist type nozzle. A thin layer of Nafion ionomer was deposited on the top of the catalyst layer by ultrasonic spray, to help the adhesion of the GDE to the membrane during the hot pressing and reduce the electrode/membrane contact resistance [45].

Then the Pt/C anode GDE was hot pressed on a Nafion N211 membrane (Ion Power Inc.) at 120 °C and 4 MPa for 5 min, to form a half-MEA. After cooling down at room temperature, the half-MEA was placed onto a vacuum sealed plate heated at 95 °C, and the cathode catalyst ink was deposited on the membrane with a paint brush to achieve a catalyst loading of ca.  $4 \text{ mg cm}^{-2}$ . The thickness of the CCL was measured with a micrometer, and it was consistently of  $100 \pm 5 \mu\text{m}$ . Assuming a density of the CCL (typical for carbon-based electrodes) of ca.  $0.4 \text{ g cm}^{-3}$  [12], the loading of ca.  $4 \text{ mg cm}^{-2}$  was confirmed.

The MEAs for mass transport resistance measurements were prepared as described above, except that a Pt black (PtB, TEC90300, TKK Corp., Japan) layer with a loading of  $0.8 \text{ mg}_{Pt} \text{ cm}^{-2}$  was deposited by ultrasonic spray coating on the cathode side of the MEA before the deposition of the PGM-free catalyst [27,44].

The loading for all Pt catalyst layers was verified by X-ray fluorescence spectroscopy (XRF) using a Fischer FISCHERSCOPE® X-RAY XDV®-SDD instrument.

### 2.2. MEA testing

For PEFC testing, all the MEAs were assembled in a  $5 \text{ cm}^2$  cell hardware with 14 parallel straight channels flow field [46], by placing a piece of SGL 29BC GDL on the cathode side without hot pressing. PTFE gaskets (127  $\mu\text{m}$  and 254  $\mu\text{m}$  on anode and cathode sides, respectively) were used to obtain a GDL compression of ca. 25%, and the cell was tightened to 40 inch-lbs.

The cell was then connected to a Hydrogenics fuel cell test station. Ultra-high purity gases (General Air, Commerce City, Colorado, USA) were used for all the tests.  $N_2$  was flown on anode and cathode while heating the cell up to 80 °C. Then the anode gas was switched to  $H_2$  and the cathode gas was switched to air, and the cell open circuit voltage (OCV) was monitored until it reached a stable value. After waiting at least 20 min for the cell conditions (temperature, pressure, and relative humidity) to equilibrate and reach steady state, polarization

measurements were performed. The polarization curves were measured at 80 °C at different relative humidity (RH) values of 50, 75, and 100%, adjusting the total cell pressure to have 100 kPa gas partial pressure ( $\text{H}_2$  on anode, and air or  $\text{O}_2$  on cathode). The gas flow rates were set to 1.0 L  $\text{min}^{-1}$  on both anode and cathode for all the tests, to assure high stoichiometry, and hence differential cell conditions with the flow field used. The polarization curves were recorded in voltage control mode starting from OCV, with a hold time of 75 s per point.

### 2.3. Electrochemical diagnostics

CV of the MEAs cathode were measured under  $\text{H}_2/\text{N}_2$  (anode/cathode gas flows at 100 mL  $\text{min}^{-1}$ ) at 80 °C and different RH values (20, 50, 75, 90, and 100%) between 0.0 and 1.0 V at 20 mV  $\text{s}^{-1}$ , adjusting the total cell pressure to keep the gas partial pressure to 100 kPa, avoiding reference shifts due to the variation of  $\text{H}_2\text{O}$  partial pressure when changing the RH. The CCL capacitance was calculated from CV data as described in Section 3.3.

EIS of the MEAs cathode were measured under  $\text{H}_2/\text{N}_2$  (anode/cathode gas flows at 100 mL  $\text{min}^{-1}$ ) at 80 °C and different RH values (20, 50, 75, 90, and 100%) in potentiostatic mode at 0.2 V, with 3 mV AC amplitude, between 100 kHz and 0.1 Hz. The total cell pressure was adjusted when RH was changed as described before. Both CV and EIS were measured with a Gamry potentiostat/galvanostat (Model Reference 3000).

The gas mass transport resistance in the CCL was determined by HOR limiting current measurements. The cell was assembled as described in Section 2.2.

Before the HOR limiting current measurements, the cell was conditioned using a Hydrogenics fuel cell test station according to a protocol described elsewhere [47], to fully activate the platinum black (PtB) layer. The working principle of the PtB sensor layer for the measurement of the mass transport resistance on a PGM-free catalyst layer is described in detail in our previous work [44]. After conditioning, the cell was connected to a Teledyne Medusa fuel cell test station, the cell temperature was set to 80 °C, and a mixture of 5% of  $\text{H}_2$  in  $\text{N}_2$  was flown on both anode and cathode with a flow rate of 2.0 and 5.0 L  $\text{min}^{-1}$ , respectively.

HOR limiting currents data were measured using a Metrohm Autolab potentiostat (Model PGSTAT302 N) recording CVs at 40 mV  $\text{s}^{-1}$  between 0.05 and 0.80 V, at different RH values of 50, 75, 90, and 100%. At each RH value, CVs were measured at 4 different cell pressures: 150, 200, 250, and 300 kPa. The HOR limiting current values were then used to extract the gas mass transport resistance, after subtracting the background CV measured flowing  $\text{N}_2$  on the cathode, as described in our previous works [27,44].

### 2.4. Nano-CT

Following the procedure described in the work of Cetinbas et al. [48], sulfonic acid groups of the ionomer in the electrode samples were ion exchanged with  $\text{Cs}^+$ . The electrode layers were sectioned into flakes to fit into the field of view (50  $\mu\text{m}$ ) and mounted on the tomography needle. X-ray radiographs were acquired at 8 keV using the Xradia nano XCT-S100 TXM at beam line 32-ID-C of the Advanced Photon Source (APS) at Argonne National Laboratory (ANL). With 0.5 s exposure time, 1080 projection images were recorded over 180° rotations and reconstructed into a 3D image sequence with 20 nm voxel size as described in Ref. [48]. Samples were scanned in both absorption and phase contrast modes. The phase contrast mode resolves the overall morphology of the secondary pores and the solid material (a mixture of catalyst, ionomer and pores below resolution), while the absorption contrast images provide an intensity map of the high electron-density materials within the sample (i.e.,  $\text{Cs}^+$  indicating the ion exchanged ionomer).

### 2.5. Electron microscopy

For electron microscopy analysis, as-prepared MEAs were embedded in Araldite 6005 epoxy resin and cured at 60 °C for 16 h. Then trimming and ultramicrotomy were done using a 36° clearance angle Diatome diamond knife. The MEA cross sections obtained were ca. 70 nm thick. Images of cross-sectioned MEAs were acquired on a FEI Talos F200X electron microscope operated at 200 keV using the STEM mode with bright field (BF) image production and coupled with EDS mapping of F element.

### 2.6. Ink properties measurements

#### 2.6.1. Rheology

Rheological measurements were performed using a stress-controlled rheometer (HAAKE MARS 60, ThermoFisher Scientific) with a stainless-steel parallel plate geometry (35 mm diameter) with a gap of 500  $\mu\text{m}$  at 25 °C. A solvent saturation trap was used in order to minimize any solvent evaporation during measurements. Prior to making measurements, the samples were preconditioned to erase any sample loading history on the microstructure by conducting a pre-shear at 500  $\text{s}^{-1}$  for 60 s and then allowed to rest for 60 s. The steady shear rheology measurements were performed by imposing a decreasing stress sweep with logarithmic spacing. The stress limits were adjusted on an individual sample basis within the range of 40 to 0.0001 Pa. In the inks for rheological study, Nafion D2020 (1000 EW, Ion Power) was used. In order to better observe the differences in agglomeration, rheology measurements were carried out on more concentrated inks (5 wt % catalyst) compared to the inks used to fabricate the MEAs (ca. 2.8 wt %), where the agglomeration effects are more significant. The inks were dispersed by ball milling for 12 h with high-density zirconia beads in glass jars.

#### 2.6.2. Dynamic light scattering (DLS)

DLS measurements on ionomer dispersions were performed using a Zetasizer Nano ZS (Malvern Instruments Ltd, Malvern, UK). All the measurements were performed at 25 °C using a disposable cuvette-cell. At least five measurements were taken to ensure repeatability of the results. The ionomer concentrations are more dilute (0.024 wt%) compared to their concentration in the inks as required by the technique to avoid multiple scattering events in the measurements.

#### 2.6.3. Ultra-small angle X-ray scattering (USAXS)

The USAXS-SAXS study of particle and agglomerate size in dispersed catalyst inks was conducted at beamline 9ID-C at Advanced Photon Source (APS), Argonne National Laboratory. The ink samples followed by sonication were collected into a glass capillary tube (1 mm diameter) and sealed with an epoxy resin. The capillary tubes were completely filled with the catalyst inks using hypodermic needles from the bottom to prevent the formation of bubbles of air which interferes with the X-ray scattering measurements. The background scattering data from the glass capillary tube filled with the solvent solution were recorded and subtracted from scattering data for each sample. The samples were exposed to a monochromatic X-ray beam in the operational energy range from 10 to 24 keV. The scattered X-ray intensity was measured over the USAXS-SAXS scattering angle ranges using a Bonse-Hart camera for USAXS and a Pilatus 100 K detector for pinhole SAXS [49]. The X-ray intensity data were collected in scattering angle ranges of  $1 \times 10^{-4}$  to  $3 \times 10^{-1} \text{ Å}^{-1}$  for the USAXS and  $4 \times 10^{-2}$  to  $1.6 \text{ Å}^{-1}$  for the pinhole SAXS. The X-ray scattering data were analyzed in the data analysis macro package Irena (Jan Ilavsky, APS, beamline 9ID-C) on the Igor Pro (WaveMetrics, OR) platform with simulations of scattering fitting functions [50].

### 3. Results and discussion

#### 3.1. Fuel cell performance

Three MEAs having 0, 50 and 82 wt% H<sub>2</sub>O (note: wt% H<sub>2</sub>O =  $100 \cdot m_{H_2O} / (m_{H_2O} + m_{nPA})$ ) were fabricated using identical methodology (ink processing and deposition), catalyst material, catalyst loading, and ionomer content in the CCL (35 wt%), limiting any differences in performance to the effect of the ink composition. The H<sub>2</sub>/air polarization curves measured at 100 and 75% RH are shown in Fig. 1. Here, error bars represent the standard deviation between two different MEAs and demonstrate the good reproducibility of the results. In Fig. 1a the H<sub>2</sub>/air polarization curves at 100% RH show a clear increase of performance with increasing H<sub>2</sub>O content, with the MEA prepared using only nPA have a 200 mV lower cell voltage at ca. 0.8 A/cm<sup>2</sup>.

At 75% RH, however, the relative performances of the MEAs leads to changes in the performance trend (see Fig. 1b). Here, the MEA prepared with a 50% H<sub>2</sub>O content in the ink shows the highest performance, with the 0% and 82% H<sub>2</sub>O content MEAs performing similarly to each other but more poorly. Much like the H<sub>2</sub>/air performance, the H<sub>2</sub>/O<sub>2</sub> polarization curves in Figs. S1a and b show a similar trend of increasing performance with increasing ink water content at 100% RH and converging performance at 75% RH for all MEAs regardless of the ink water content. Overall, the performance difference for both H<sub>2</sub>/air and

H<sub>2</sub>/O<sub>2</sub> at 75% RH is significantly smaller than at 100% RH, though from polarization data alone it is difficult to describe the potential trade-off in voltage losses causing such an effect. Note that regardless of the ink solvent composition, the three different MEAs show a similar performance decay trend, which is in the order of ca. 10% at intermediate current density values (i.e. around 0.4 V, see Fig. S2).

These results indicate that the ink H<sub>2</sub>O/nPA content impacts the resulting electrode structure and its consequent electrochemical properties, resulting in a considerably different MEA performance. Specifically, the electrode prepared with the 82 wt% H<sub>2</sub>O is the most influenced by RH, though piecing together structural information of the electrode requires direct measurements of bulk-electrode gas transport, electrochemical capacitance and catalyst layer proton transport, as is done in following Sections 3.2 – 3.3 – 3.4.

#### 3.2. Bulk-electrode gas transport measurements

The total bulk-electrode gas transport resistance ( $R_{total}$ ) for the different CCLs, determined from HOR limiting current measurements, was calculated according to Equation (1) [27,44]:

$$R_{measured} = R_b + R_{total} = \frac{nFC_{H_2, channel}}{i_{lim} - i_x - i_{CV}} \quad (1)$$

Where  $R_{measured}$  is the measured transport resistance through the entire cell,  $R_b$  is the background resistance in the absence of a PGM-free catalyst layer,  $n$  is the number of electrons transferred by reaction,  $F$  is Faraday's constant,  $C_{H_2, channel}$  is the H<sub>2</sub> concentration in the flow field channel,  $i_{lim}$  is the measured limiting current,  $i_x$  is the crossover current, and  $i_{CV}$  is the background capacitive current measured flowing N<sub>2</sub> on the cathode. For these measurements, the PGM-free CCL was deposited on the top of a PtB sensor layer and the data acquired and processed in identical fashion to previously published methodology [44]. The HOR limiting currents for the three different CCLs measured at 80 °C, 150 kPa and 50, 75, 90 and 100% RH (Fig. S3a, c and e) along with the resulting  $R_{total}$  values (Fig. S3b, d and f) are shown in the Supplementary Information. The values of  $R_{total}$  are summarized in Fig. S4 for easier comparison between MEAs and relative humidity. For each CCL,  $R_{total}$  increases with pressure at a given RH, while at constant cell pressure,  $R_{total}$  increases with RH.

Fig. 2a shows the latter scenario at 150 kPa cell pressure, where regardless of the fabrication conditions,  $R_{total}$  increases with RH. Perhaps more interesting and insightful is the dependence of  $R_{total}$  in Fig. 2a on ink water content across all RHs. These values are also summarized in Table 1 (see Section 3.4).  $R_{total}$  depends on the relative H<sub>2</sub>O/nPA content in the ink. Specifically, the CCL fabricated with nPA-rich ink (0 wt% H<sub>2</sub>O) shows  $R_{total}$  values ca. 2.2–2.5 times than the CCL fabricated with 50 wt% H<sub>2</sub>O ink, and 5.5–6 times higher than the CCL fabricated with the H<sub>2</sub>O-rich ink (82 wt% H<sub>2</sub>O).

Moreover, the degree to which  $R_{total}$  varies with RH also changes as a function of the ink water content. This dependence is depicted more clearly in Fig. 2b, where the pressure independent component of the bulk-electrode gas transport resistance ( $R_{NP}$ , ordinate axis intercept values from Fig. S3 b, d, and f [27,44,46]) is plotted as function of the RH. Breaking up the total bulk-electrode resistance into the pressure dependent ( $R_p$ , slope of Fig. S3 b, d, and f) and independent terms ( $R_{NP}$ ) allows one to determine the resistance contributions stemming from molecular diffusion ( $R_p$ , occurring in pores larger than ca. 20 nm) as compared to Knudsen diffusion through smaller pores in combination with diffusion through ionomer films ( $R_{NP}$ ). Clearly, there is a cause/effect relationship between  $R_{NP}$  and  $R_p$  since they occur in both parallel and series throughout the thickness of the electrode and observed changes in  $R_{NP}$  can be useful in gleaning information about the electrode structure.

Increasing RH increases water uptake, causing the ionomer to swell and reduce the available pore volume of the electrode [51,52]. This has

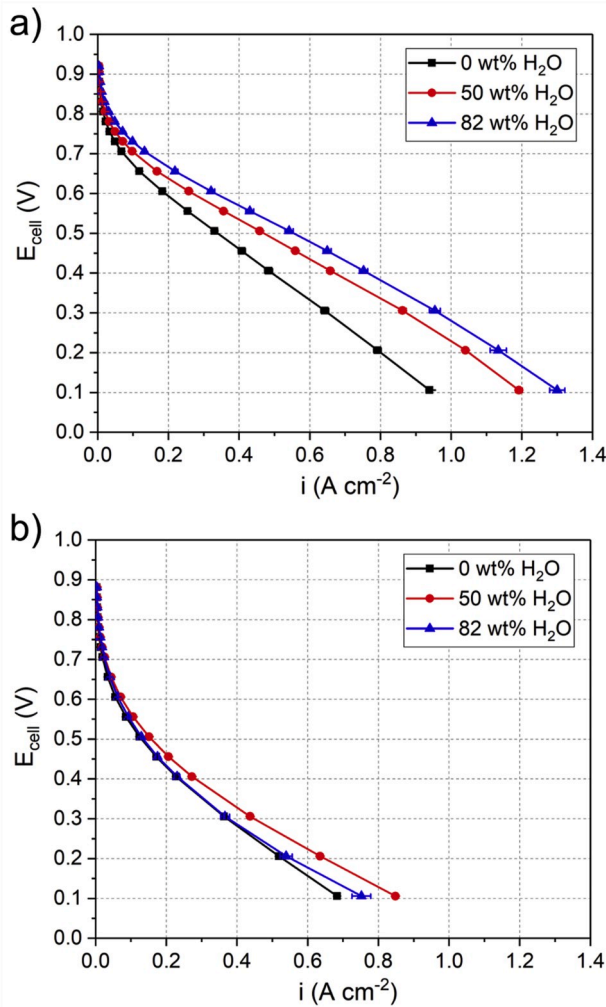
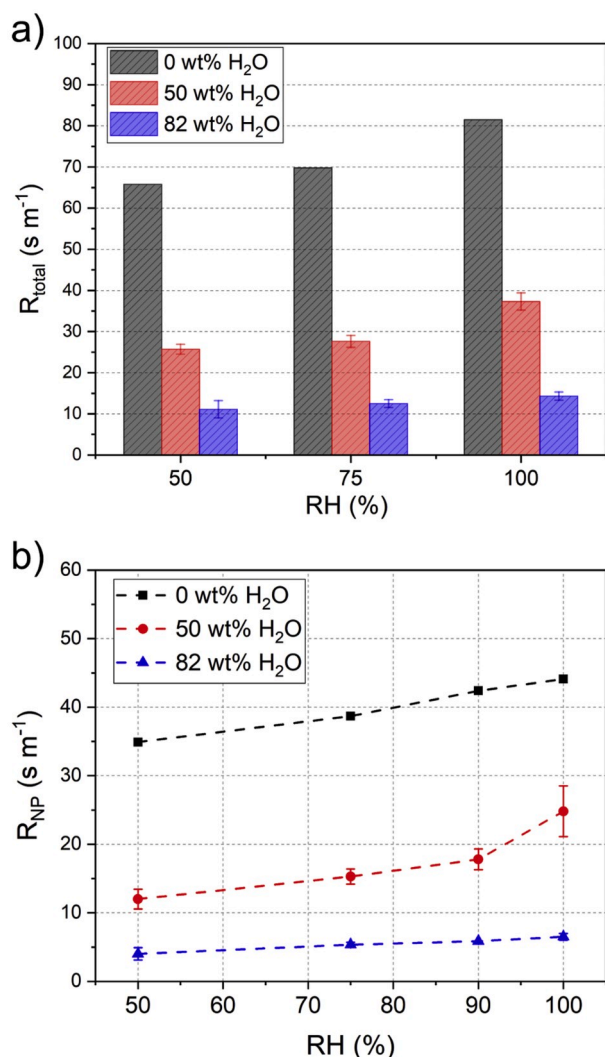


Fig. 1. H<sub>2</sub>/air polarization curves measured at 80 °C and 100 kPa gas partial pressure for MEAs fabricated with different H<sub>2</sub>O contents in the ink solvent. (a) 100% RH; (b) 75% RH.





**Fig. 2.** (a) Total bulk-electrode gas transport resistance measured at 80 °C and 150 kPa and (b) pressure independent resistance at 50, 75 and 100% RH for the three CCLs prepared with inks containing 0, 50 and 82 wt% H<sub>2</sub>O.

a deleterious effect particularly for smaller pores in which Knudsen diffusion dominates. Here, as ionomer occupies more pore volume and pore diameters correspondingly shrink, the Knudsen diffusivity of the probe gas, in this case H<sub>2</sub>, is decreased proportionally according to Equation (2). Here,  $D_{Kn}$  is the Knudsen diffusivity,  $R$  is the universal gas constant,  $T$  is temperature, and  $M$  is molecular mass.

$$D_{Kn} = \frac{d_{pore}}{3} \sqrt{\frac{8RT}{\pi M}} \quad (2)$$

It should be noted that the increase in  $R_{NP}$  with increasing RH for

bulk-electrode transport observed here is different from the aggregate level diffusion resistance decrease with increase of RH observed in the work of Ahluwalia et al. [37], where the transport losses in a PGM-free CCL were modeled from polarization curves data. In the work of Ahluwalia et al. the solid-state diffusion of O<sub>2</sub> through ionomer films surrounding the electrocatalyst aggregates was shown to decrease with RH, highlighting the need to differentiate between bulk electrode, aggregate level, and near active site limitations. Nevertheless, the increases in  $R_{NP}$  for bulk-electrode transport shown here, coupled with the parallel and series pathways of  $R_p$  and  $R_{NP}$ , can result in an increased path length for molecular diffusion depending on the initial electrode structure. Since the three CCLs examined in this work have the same ionomer content, any observed differences in  $R_{NP}$ ,  $R_p$  and  $R_{total}$  along with their respective dependence on RH, would be related to the impact of ink formulation on pore size distribution and connectivity stemming from variations in ionomer distribution within the CCL, catalyst/ionomer aggregation, or a combination thereof. These proposed variations in electrode morphology and component interactions are further investigated in the subsequent sections.

### 3.3. Electrode capacitance

CV data were collected at different RH values (from 25 to 100%) for the three different CCLs (see Fig. S5 in the Supplementary Information) to determine how RH and the accumulation of liquid water via capillary condensation impacts electrochemical capacitance. The capacitive current measured by CV is a combination of various effects such as, catalyst surface area, catalyst electrical conductivity, ionomer distribution, catalyst-ionomer interactions, pore geometry and size distribution, and presence of electrochemically active functional groups on the catalyst surface. As RH is changed the relative interactions of ionomer and water with the electrocatalyst surface will change depending on the initial distribution of ionomer and the pore structure of the electrode. For example, in situations where the ionomer is more homogeneously and conformally coating the electrocatalyst surface, one would expect a minimal change in capacitance with RH. Here, electrode capacitance ( $C$ ) was calculated using Equation (3):

$$C = \frac{i_{CV,+}^{0.4V} + |i_{CV,-}^{0.4V}|}{2\nu} \quad (3)$$

Where  $\nu$  is the scan rate, and  $i_{CV,+}^{0.4V}$  and  $i_{CV,-}^{0.4V}$  are the current density measured at 0.4 V in the positive and negative scan directions, respectively. For all the MEAs, the shape of the CVs is quasi-rectangular, with the presence of a reversible redox peak in the potential region between 0.70 and 0.85 V, as commonly observed for this class of Fe–N–C electrocatalysts in both MEA and liquid electrolyte [21,24,53–56]. The peak is associated with the redox behavior of atomically dispersed Fe–N<sub>x</sub> moieties, found to be the active sites for ORR in acidic medium [21,55,57,58].

For all CVs in Fig. S5, the capacitance increases with the RH. This is explained by both an increased wetting of the electrocatalyst surface and pores with increasing RH [39,59], and perhaps to a lesser extent, increased ionomer catalyst/interactions due to enhanced ionomer

**Table 1**

Electrode parameters measured by the electrochemical diagnostics techniques at different RH: capacitance ( $C$ ), proton resistance ( $R_{\Omega}^c$ ), and total mass transport resistance at 150 kPa ( $R_{total}$ ).

CCL ink	0 wt% H <sub>2</sub> O			50 wt% H <sub>2</sub> O			82 wt% H <sub>2</sub> O		
RH (%)	C (mF cm <sup>-2</sup> )	R <sub>Ω</sub> <sup>c</sup> (mΩ cm <sup>2</sup> )	R <sub>total</sub> (s m <sup>-1</sup> )	C (mF cm <sup>-2</sup> )	R <sub>Ω</sub> <sup>c</sup> (mΩ cm <sup>2</sup> )	R <sub>total</sub> (s m <sup>-1</sup> )	C (mF cm <sup>-2</sup> )	R <sub>Ω</sub> <sup>c</sup> (mΩ cm <sup>2</sup> )	R <sub>total</sub> (s m <sup>-1</sup> )
25	27.0	–	–	40.1	–	–	39.6	–	–
50	46.4	240	65.8	61.9	427.5	25.7	77.8	832.5	11.1
75	71.8	145	69.8	89.4	275	27.6	135.9	527.5	12.5
90	100.1	115	75.7	100.0	175	30.7	157.9	395	13.1
100	110.0	85	81.5	101.5	145	37.3	171.6	255	14.3

swelling [60]. Table 1 summarizes the capacitance values at different RH for the three CCLs. The CCL fabricated with 50 wt% H<sub>2</sub>O ink has slightly higher  $C$  values compared to the CCL with 0 wt% H<sub>2</sub>O ink at low RH, but then at high RH (90 and 100%) their  $C$  values are again very similar. In order to more accurately contrast the relative changes in capacitance between the three electrodes fabricated with different ink water content, Fig. 3 plots the normalized capacitance ( $C_N$ ), defined as the capacitance at a given RH, divided by the capacitance at 100% RH.

In Fig. 3, both the 82 wt% and 0 wt% H<sub>2</sub>O electrodes show a steeper normalized  $C$  decrease with RH compared to the 50 wt% H<sub>2</sub>O electrode, both having a  $C_N$  value of ca. 0.4 at 50% RH, and ca. 0.25 at 25% RH. On the other hand, the electrode with 50% H<sub>2</sub>O shows a less steep variation with RH. While increased capacitance at low RH does not linearly translate to available active-sites in the same way that electrochemical surface area determined at low RH via CO stripping does for PGM-based electrocatalysts/electrodes [61], when the same electrocatalyst is involved, the retention of higher capacitive values certainly means a higher probability of enabling a reaction at an electrochemical triple-phase boundary. Consequently, the enhanced capacitive robustness of the PGM-free electrode fabricated with the 50 wt% H<sub>2</sub>O ink is visible in the low RH polarization data in (see Figs. 1b and S1b), where the best performance is obtained by the MEA with 50% H<sub>2</sub>O ink.

Coupling the information from measurements of bulk-electrode gas transport resistance and electrode capacitance, it may be inferred that the ionomer distribution as well as ionomer and electrocatalyst aggregation are significantly impacted by the ink water content.

### 3.4. Electrode proton conductivity

While the capacitive results from the previous section yield information on ionomer interactions near the electrocatalyst surface, EIS data can be used to understand information regarding the connectivity of ionomer pathways for proton transport. As such, Nyquist plots of the EIS measured on the three CCLs at 100% RH in H<sub>2</sub>/N<sub>2</sub> operating mode, are shown in Fig. 4.

For PEFC electrodes, the Nyquist plot of the EIS data measured in H<sub>2</sub>/N<sub>2</sub>, with no background faradaic reactions, has a ca. 45° slope shape in the high frequency region, which then sharply approaches an asymptotic vertical trend at low frequencies (pure capacitive response) [62, 63]. This EIS shape can be fit using the transmission line equivalent circuit model [40,41,43]. This model has been successfully applied to fit EIS data for conventional (ca. 10  $\mu$ m thick) Pt/C electrodes [43,64] as

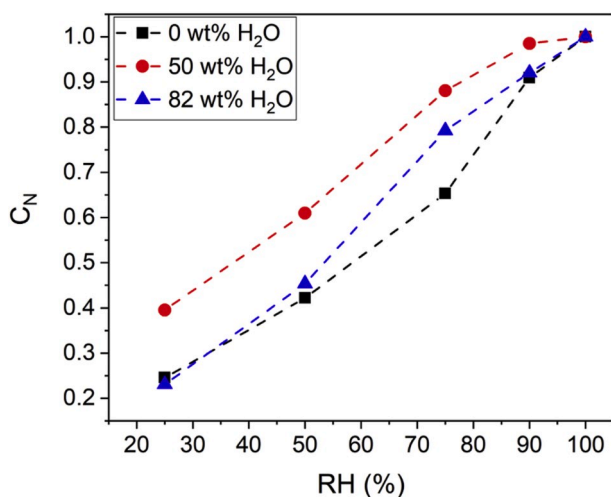


Fig. 3. Dependence of the CCL normalized capacitance ( $C_N$ ) on the RH for the MEAs prepared with three different H<sub>2</sub>O contents in the ink. Normalized capacitance  $C_N$  is defined as the capacitance at a given RH, divided by the capacitance at 100% RH.

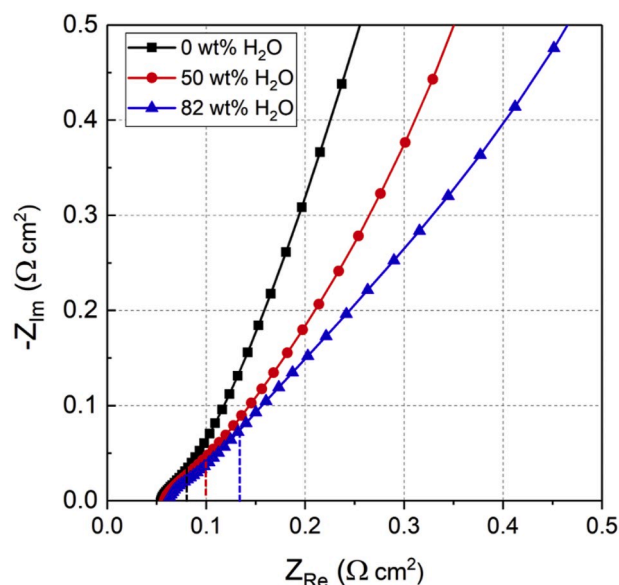


Fig. 4. H<sub>2</sub>/N<sub>2</sub> EIS Nyquist plot of CCL fabricated with inks containing different wt% of H<sub>2</sub>O measured at 100%RH. The dashed lines represent the limit of the ca. 45° slope region used to identify the electrode proton transport resistance.

well as PGM-free electrodes with a lower catalyst loading [27], and a homogeneous particle morphology [21]. In the present study, however, this model did not fit properly the EIS data shown in Fig. 4. The transmission line model (semi-infinite Warburg diffusion + pure capacitance) requires homogeneous planar particles with consistent ionomer coverage, each representing a rung in the transmission line ladder model. However, for electrodes having heterogeneous particle morphology both in shape and size, and/or heterogeneous ionomer distributions on said particles, a more refined model is necessary to accurately fit the experimental data [62,63,65,66]. While there are limitations/deficiencies to using a transmission line model for these MEAs, it still provides a reasonable approximation of the electrode proton transport resistance ( $R_{\Omega}^c$ ).

While the Nyquist plot in Fig. 4 do not show a sharp transition from a 45° region to a vertical region for the aforementioned reasons [62], a more subtle transition is present in all plots, becoming more abrupt at higher RH (see also Fig. S6 for data at lower RH values). Given all the limitations previously described,  $R_{\Omega}^c$  values are listed in Table 1 and should be utilized as a means of relative comparison between the CCLs examined in this study, rather than as correct and precise values.

From Figs. 4 and S6 and the values in Table 1, it is evident that  $R_{\Omega}^c$  increases with the decrease of RH due to the decrease of the ionomer conductivity and commensurate drying of electrode pores, which may cause limited proton conduction over short length scales. Also, at all RH values, the electrodes show a clear dependence on ink H<sub>2</sub>O content, where  $R_{\Omega}^c$  increases with increasing wt% H<sub>2</sub>O. Recent literature has pointed out a significant impact of ionomer thickness on conductivity [67,68]. In addition, changes in ionomer conformation and aggregation as a function of ink water content during ink formation and drying [69, 70], and in the resulting electrode structure [31], have been demonstrated. For these reasons, there are many superimposed factors influencing the observed differences in  $R_{\Omega}^c$ .

However, the behavior of the bulk ionomer should not be confused with the ionomer-catalyst near surface interactions. In fact, while the 0 wt% H<sub>2</sub>O fabricated electrode had the most rapid decrease in capacitance with RH, losing ca. 35% of its capacitance at 75% RH (see Fig. 3), it has the most moderate increase in  $R_{\Omega}^c$  at 75% RH (see Table 1). These observations are not contradictory, but synergistic. If the ionomer is not associated with the electrocatalyst surface, as indicated by the capacitive measurements, it is then preferentially occupying the electrode

bulk, allowing for improved proton conductivity, while at the same time making the electrode more susceptible to bulk-electrode transport losses. This is shown explicitly in Fig. 2a and implicitly by the reduced performance in Fig. 1, and further investigated using microscopy and tomography in Section 3.5.

### 3.5. Electrode structure analysis: STEM/EDS and Nano-CT

For three-dimensional characterization of the electrode morphology, we acquired nano-CT images of the different ink composition CCLs. Nano-CT analysis provides information about the electrode microstructure at 20-nm voxel resolution in terms of solid electrode material (including ionomer distribution relying on absorption contrast images of Cs stained electrodes) and pore space; and can be used to calculate effective transport properties within the electrode [48,71–74].

The volume render of the segmented phase contrast images in Fig. 5a–c shows the overall structural morphology of the scanned electrodes. They consist of large solid particles (containing primary pores in them) separated by the secondary pore space. The visual inspection of Fig. 5a–c indicates that the electrode prepared with 0 wt% H<sub>2</sub>O ink has smaller particles and smaller secondary pores (also see Fig. S7 for cross sections). Increasing the H<sub>2</sub>O content in the ink causes an increase in the size of the secondary pores as quantitatively confirmed in Fig. 5d. The inset plot in Fig. 5d shows the mean pore diameter. A decrease from a mean diameter of ca. 570 nm for the 82% H<sub>2</sub>O electrode, down to 420 nm for the 0% H<sub>2</sub>O one was calculated, with an intermediate value of ca. 510 nm for the 50% H<sub>2</sub>O electrode.

The effective gas diffusion coefficients ( $D_{\text{eff}}$ ) inside the CCLs were calculated using the nano-CT data, according to the method described in the work of Cetinbas et al. [48], and reported in Table 2. It is important to note that nano-CT determined  $D_{\text{eff}}$  are at 0% RH since they are determined ex-situ and as such, the calculations do not consider water generation inside the CCL during operation, nor local ionomer swelling.

Using the  $D_{\text{eff}}$  values, and assuming an approximate thickness of ca. 100  $\mu\text{m}$  for all the electrodes (confirmed by the cathode catalyst loading measurements, see Section 2.1), the effective mass transport resistances ( $R_{\text{total}}$ ) were also calculated and can be compared with the values

reported in the literature for other PGM-free CCLs. All the values are summarized in Table 2.

Comparing the  $R_{\text{total}}$  and  $D_{\text{eff}}$  values obtained from nano-CT and from HOR limiting current experiments in Table 1, we have to consider that even though the T and P conditions are the same (80 °C, 150 kPa), the HOR limiting current values were measured at RH from 50% up to 100%. On the other hand, the  $R_{\text{total}}$  values obtained from nano-CT are obtained under conditions of 0% RH.

For the CCL with a larger average pore size (the one fabricated with 82 wt% H<sub>2</sub>O in the ink) the  $D_{\text{eff}}$  measured by nano-CT in dry conditions, is close to the  $D_{\text{eff}}$  measured at high RH by HOR limiting current. This is mainly because this electrode suffers a lower contribution of small pores for the gas diffusion. Moreover, the more uniform ionomer distribution could result in less dramatic effect of ionomer swelling. Thus, this CCL is less impacted by the water presence during operation. On the other hand, for the CCLs having smaller pore size (the ones fabricated with nPA-richer inks), the  $D_{\text{eff}}$  values measured by nano-CT differ more from the ones measured at high RH by HOR limiting current due to the more predominant presence of narrow pores that more easily obstruct the diffusion of gas molecules when the water content in the electrode increases. This comparison is depicted in Fig. 6.

Fig. S7a–c–e show the cross sections of raw phase contrast images of the three electrodes, and Fig. S7b–d–f are the absorption contrast images where the green color represents the Cs<sup>+</sup> stained ionomer. The ionomer is more homogeneously distributed inside the catalyst particles and agglomerates for the 82 and 50 wt% H<sub>2</sub>O CCLs, while for the 0 wt% H<sub>2</sub>O CCL the ionomer does not infiltrate into large particles/agglomerates and accumulates preferentially on the catalyst agglomerates surface and in between them. These observations agree with the STEM-EDS results in Fig. 7, which shows the EDS mapping of the F element (in green color), clearly indicating the distribution of ionomer.

The three CCLs appear considerably different in terms of ionomer distribution and infiltration within the pores between catalyst particles. In the CCL prepared with 0 wt% H<sub>2</sub>O ink, the ionomer seems to cover the catalyst particles less homogeneously, and ionomer chunks as thick as several hundred nm are observed between large particles (Fig. 7a), in agreement with the higher  $R_{\text{total}}$  and lower  $R_{\text{O}_2}^c$  measured for this CCL.

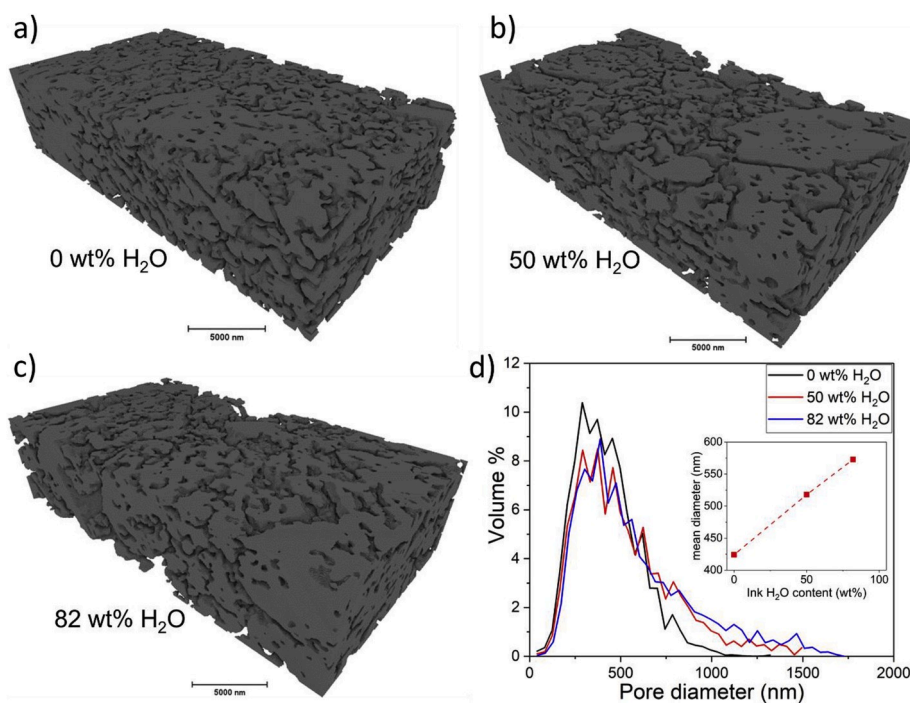


**Fig. 5.** Nano-CT segmented phase contrast images for the CCL prepared with different water content in the ink: (a) 0 wt% H<sub>2</sub>O; (b) 50 wt% H<sub>2</sub>O; (c) 82 wt% H<sub>2</sub>O. (d) Pore diameter distribution of the three different electrodes. The inset shows the average pore diameter in function of the water content in the ink.



**Table 2**  
Mass transport resistance and effective diffusion coefficients values for H<sub>2</sub> and air for the three different MEAs analyzed in this work, calculated from nano-CT at 150 kPa and 80 °C, and from HOR limiting current experiments. The values are compared with other reported in the literature for PGM-free electrodes fabricated with different methods. US = hand painting.

Catalyst loading	Solvent content	Ink deposition method	Ionomer content	Electrode thickness	75% RH						90% RH						100% RH						Ref.
					R <sub>total</sub>	D <sub>eff</sub>	D <sub>eff</sub>	D <sub>eff</sub>	D <sub>eff</sub>	D <sub>eff</sub>	R <sub>total</sub>	D <sub>eff</sub>	D <sub>eff</sub>	D <sub>eff</sub>	D <sub>eff</sub>	D <sub>eff</sub>	R <sub>total</sub>	D <sub>eff</sub>	D <sub>eff</sub>	D <sub>eff</sub>	D <sub>eff</sub>	D <sub>eff</sub>	
(mg cm <sup>-2</sup> )	(H <sub>2</sub> O:nPA)		(wt%)	(μm)	(s m <sup>-1</sup> )	(x10 <sup>6</sup> m <sup>2</sup> s <sup>-1</sup> )	(x10 <sup>6</sup> m <sup>2</sup> s <sup>-1</sup> )	(x10 <sup>6</sup> m <sup>2</sup> s <sup>-1</sup> )	(x10 <sup>6</sup> m <sup>2</sup> s <sup>-1</sup> )	(x10 <sup>6</sup> m <sup>2</sup> s <sup>-1</sup> )	(s m <sup>-1</sup> )	(x10 <sup>6</sup> m <sup>2</sup> s <sup>-1</sup> )	(x10 <sup>6</sup> m <sup>2</sup> s <sup>-1</sup> )	(x10 <sup>6</sup> m <sup>2</sup> s <sup>-1</sup> )	(x10 <sup>6</sup> m <sup>2</sup> s <sup>-1</sup> )	(x10 <sup>6</sup> m <sup>2</sup> s <sup>-1</sup> )	(s m <sup>-1</sup> )	(x10 <sup>6</sup> m <sup>2</sup> s <sup>-1</sup> )	(x10 <sup>6</sup> m <sup>2</sup> s <sup>-1</sup> )	(x10 <sup>6</sup> m <sup>2</sup> s <sup>-1</sup> )	(x10 <sup>6</sup> m <sup>2</sup> s <sup>-1</sup> )	(x10 <sup>6</sup> m <sup>2</sup> s <sup>-1</sup> )	
2	4:6	US	30	45	22	2.07	0.72	0.59	0.54	0.54	29	1.56	0.54	0.54	0.54	0.54	29	1.56	0.54	0.54	0.54	0.54	[44]
2	4:6	US	45	45	88	0.51	0.18	0.16	0.15	0.15	103	0.46	0.16	0.15	0.15	0.15	103	0.46	0.16	0.15	0.15	0.15	[44]
4	4:6	US	30	90	31	2.88	0.99	0.87	0.73	0.73	36	2.52	0.87	0.73	0.73	0.73	36	2.52	0.87	0.73	0.73	0.73	[44]
2	4:6	US	30	50	22	2.28	0.79	0.71	0.64	0.64	24	2.06	0.71	0.64	0.64	0.64	27	1.85	0.64	0.64	0.64	0.64	[27]
2	4:6	US	35	50	42	1.20	0.42	0.35	0.31	0.31	50	1.01	0.35	0.31	0.31	0.31	56	0.89	0.31	0.31	0.31	0.31	[27]
2	4:6	US	40	50	65	0.77	0.27	0.23	0.20	0.20	74	0.67	0.23	0.20	0.20	0.20	85	0.59	0.20	0.20	0.20	0.20	[27]
2	4:6	US	45	50	104	0.48	0.17	0.14	0.11	0.11	121	0.41	0.14	0.11	0.11	0.11	158	0.32	0.11	0.11	0.11	0.11	[27]
4	0:1	HP	35	100	70	1.43	0.49	0.46	0.42	0.42	76	1.32	0.46	0.42	0.42	0.42	82	1.23	0.42	0.42	0.42	0.42	this work
4	1:1	HP	35	100	28	3.62	1.25	1.12	0.92	0.92	31	3.26	1.12	0.92	0.92	0.92	37	2.68	0.92	0.92	0.92	0.92	this work
4	8:2	HP	35	100	13	8.00	2.76	2.63	2.41	2.41	13	7.63	2.63	2.41	2.41	2.41	14	6.99	2.41	2.41	2.41	2.41	this work

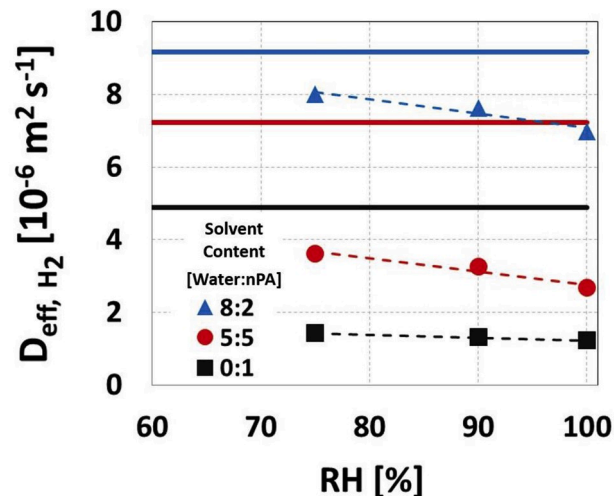


**Fig. 6.** Comparison between the  $D_{eff}$  values obtained from nano-CT at 0% RH (solid lines) and the  $D_{eff}$  values measured by HOR limiting current experiments at different RH (dashed lines/symbols), for the CCLs fabricated with different ink formulations: 0 wt% H<sub>2</sub>O (black squares); 50 wt% H<sub>2</sub>O (red circles); 82 wt% H<sub>2</sub>O (blue triangles). (For interpretation of the references to color in this figure legend, the reader is referred to the Web version of this article.)

The CCL prepared with the 50 wt% H<sub>2</sub>O ink has a better ionomer infiltration inside the small intra-particle pores (Fig. 7b). The thickness of the ionomer layer inside smaller pores is lower than 50 nm, in good agreement with the results in Fig. 3b showing a lower dependence of  $C_N$  on RH, which is an indication of a better ionomer infiltration inside the pores. The improved polarization performance under low RH conditions (Figs. 1b and S1b) also supports this result.

Finally, the CCL prepared with the 82 wt% H<sub>2</sub>O ink shows bigger catalyst agglomerates and pore size (see Fig. 7c), corroborating the lowest  $R_{total}$  and the best electrode performance in H<sub>2</sub>/air at high RH, where the mass transport limitations are higher [27,44,60]. The ionomer in this CCL appears more homogeneously distributed compared to the other two CCLs, well covering the external surface of the catalyst particles agglomerates. The ionomer layer around the particles indeed appears thin and tortuous, with fewer contact points, in agreement with the higher  $R_Q^c$  measured for this electrode.

### 3.6. Ink characterization: USAXS, rheology and DLS

To determine how the ink microstructure is influencing the CCL microstructure, ink features such as the size of catalyst particles and particles agglomerates, and the size of ionomer aggregates in the solvent were characterized by different techniques.

The effect of solvent composition on the ionomer aggregate size was investigated using DLS measurements. The ionomer aggregate size distribution in the different dispersions are shown in Fig. 8a. At both low and high H<sub>2</sub>O content (0 and 82 wt% H<sub>2</sub>O), the ionomer aggregates are predominantly large, beyond several tens of nm to μm. Whereas at 50 wt% H<sub>2</sub>O content the ionomer has a larger fraction of smaller aggregates, between 20 and 50 nm, and even below 10 nm. This is consistent with previous studies on the structure of ionomer in similar dispersion media which suggest a rod-like agglomerated structure of ionomer with radius 1–2 nm and tens of nm in length using techniques such as SAXS and cryo-TEM [75,76]. This result also explains why we observed better ionomer infiltration inside the catalyst particles for the 50 wt% H<sub>2</sub>O ink (EDS mapping in Fig. 7). Only at 50 wt% H<sub>2</sub>O the ionomer agglomerates are small enough to penetrate into the pores of the catalyst particles.

Additionally, the agglomerated structure of inks at different solvent ratios were characterized by rheology. The steady-shear relative viscosity data is compared for the different solvent compositions in Fig. 8b.



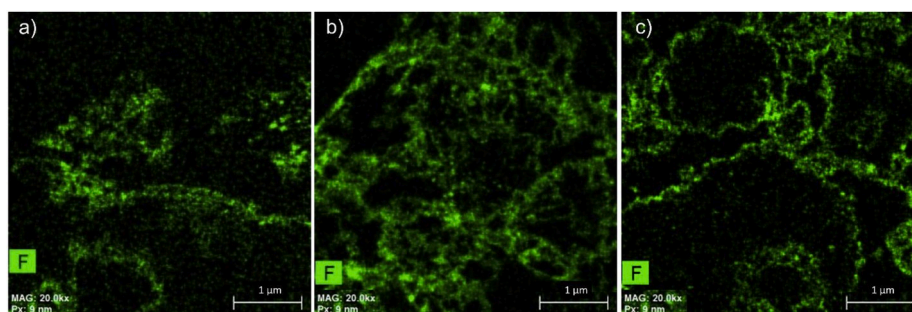


**Fig. 7.** EDS mapping of F element associated with the ionomer (green color) of the CCLs fabricated with inks containing different wt% of H<sub>2</sub>O. (a) 0 wt% H<sub>2</sub>O; (b) 50 wt% H<sub>2</sub>O; (c) 82 wt% H<sub>2</sub>O. (For interpretation of the references to color in this figure legend, the reader is referred to the Web version of this article.)

The steady-shear relative viscosity ( $\eta_r$ ) is defined as the measured viscosity ( $\eta$ ), divided by the dispersion medium viscosity ( $\eta_m$ ) which are 2.04, 2.65 and 1.59 mPa·s for 0 wt%, 50 wt% and 82 wt% H<sub>2</sub>O solvents, respectively [77]. The low-shear viscosity increases with H<sub>2</sub>O content in the ink, suggesting that the agglomerates size increases. Furthermore, the Newtonian response at 0 wt% and 50 wt% H<sub>2</sub>O suggests that agglomerates are minimal. Whereas, a shear-thinning response at 82 wt% H<sub>2</sub>O indicates the existence of a significant number of agglomerates, which are broken-down in shear flow [76]. The agglomerated structure of the ink may be dictated by the catalyst-ionomer-solvent interactions. H<sub>2</sub>O may poorly interact with the catalyst due to hydrophobic nature of the C-based catalyst, which promotes inter-particle agglomeration. Nafion has been proven to distribute and self-assemble differently onto both PGM and PGM-free catalyst surfaces depending on their hydrophobicity/hydrophilicity [78]. In addition, it has been demonstrated that Nafion can stabilize catalyst agglomerates in nPA-rich solvents by electro-steric repulsion [79]. Thus, the catalyst-ionomer interactions might be weaker in case of H<sub>2</sub>O-rich solvent, resulting in a more agglomerated ink structure in H<sub>2</sub>O-rich solvents. A more detailed investigation of ink H<sub>2</sub>O:nPA ratio effects on the agglomerated structure of these inks and the relevant interaction mechanisms is forthcoming in a separate publication.

The rheological observations were additionally verified by USAXS. Fig. 8c shows the scattered intensity ( $I(q)$ ) versus the scattering vector ( $q$ ) for the three different inks. We compared the power-law scaling exponent of the intensity at low- $q$  ( $<10^{-3} \text{ \AA}^{-1}$ ),  $I(q) \sim q^{-d_f}$ , where  $d_f$  is the mass fractal dimension.  $d_f$  represents the agglomerated structure level (mass fractal), where a larger  $d_f$  indicates a greater level of agglomeration [80,81]. The low- $q$  intensity and the  $d_f$  values for the 82 wt% H<sub>2</sub>O ink ( $d_f = 2.97$ ) is much larger than for the 50 wt% ( $d_f = 1.23$ ) and the 0 wt% H<sub>2</sub>O ( $d_f = 1.27$ ) inks by ca. 2.3 times. These data indicate that the 82 wt% H<sub>2</sub>O ink contains larger agglomerates than the inks with lower H<sub>2</sub>O content, whereas the differences in the agglomerated structure between 50 wt% and 0 wt% H<sub>2</sub>O inks appear to be not significant. Note that the rheological observations, despite being acquired at higher ink concentrations than USAXS (ca. 5 wt% vs 2.8 wt% solid content, respectively) and utilizing different ink mixing methods (ball milling instead of sonication), are in qualitative agreement with USAXS, indicating it indicates that both methods accurately capture the effect of the ink water content on the agglomerated structure of inks used to prepare the CCLs.

### 3.7. Remarks for the interpretation of fuel cell performance

The results shown here demonstrate that multiple factors determine the performance of a PEMFC CCL fabricated with a Fe–N–C catalyst and that each of these factors (bulk-electrode gas transport, proton conductivity, and electrocatalyst/ionomer interactions) may become limiting depending on the PEFC operating condition. To explain this, we must keep in mind that in the cathode of a PEFC, the ORR occurs at the triple phase boundary region [82]. While the requirement here is that O<sub>2</sub>

gas molecules must get adsorbed onto a catalyst active site, the ionic pathway can come from adsorbed water films or ionomer, with a final requirement of electronic connectivity through the catalyst carbonaceous structure [17,82–85]. Thus, a good distribution of ionomer inside the CCL is necessary to assure an effective percolative network for the conduction of the protons with a low resistance (low tortuosity, high percolating area). This feature is quantifiable by the  $R_\Omega^c$  value. Simply distributing ions throughout the electrode is not enough, however, as ionic accessibility to the active site depends on the quality of the electrocatalyst/ionomer interaction, which is qualitatively understood by measuring the normalized electrode capacitance as a function of RH.

The quality of the electrocatalyst/ionomer interaction has implications on bulk-electrode transport as well, since any ionomer not interacting with the electrocatalyst or support would be filling the electrode void and increasing bulk-electrode transport resistance.

PEFC operation at high RH favors the proton conductivity of the ionomer layer, but at the same time reduces the O<sub>2</sub> molecular diffusion. In fact, the presence of more H<sub>2</sub>O in vapor phase reduces the effective diffusion coefficient of the bulk-electrode as additional water uptake causes ionomer swelling, creating narrower pores and obstruction. On the contrary, low RH conditions limit the proton conductivity of the ionomer percolating network, but at the same time favor gas transport throughout the electrode.

Our results demonstrate that for an electrode fabricated with a specific Fe–N–C catalyst, catalyst loading, and ionomer content, the electrode structure can be tuned by varying the ink formulation in terms of nPA and H<sub>2</sub>O relative content. A certain electrode structure can be more suitable for operation under specific RH conditions, depending on which parameter (e.g. proton conductivity, mass transport resistance) is more limiting for the PEFC operation under such conditions.

Along those lines, Fig. 9a is a visual culmination of the bounty of information presented in this work, illustrating how the breakup of electrocatalyst agglomerates and electrocatalyst/ionomer interactions vary as a function of ink H<sub>2</sub>O content. Additionally, Fig. 9b depicts the manifestation of the physical properties of these electrodes as ionic and gas transport resistances. A clear tradeoff is observed between ionic and gas transport resistance as the relative humidity of the system is changed. Although this tradeoff occurs regardless of ink water content, there is a decrease in the dependency of bulk-electrode gas transport resistance on RH with increasing water content, while electrode proton resistance has increased RH dependence.

Inevitably, the MEA fabrication variables and optimum ink formulation to achieve maximum and robust fuel cell performance will vary for each different electrocatalyst morphology and functionality [21,27,28,47]. However, having explicitly shown a connection between fundamental electrochemical understanding and techniques, e.g. impedance, limiting current and cyclic voltammetry, and more advanced characterization methods, e.g. USAXS and nano-CT, we hope that this work enables those who rely solely on fundamental measurements and do not have access to advanced characterization techniques to better conceptualize their electrode structure.

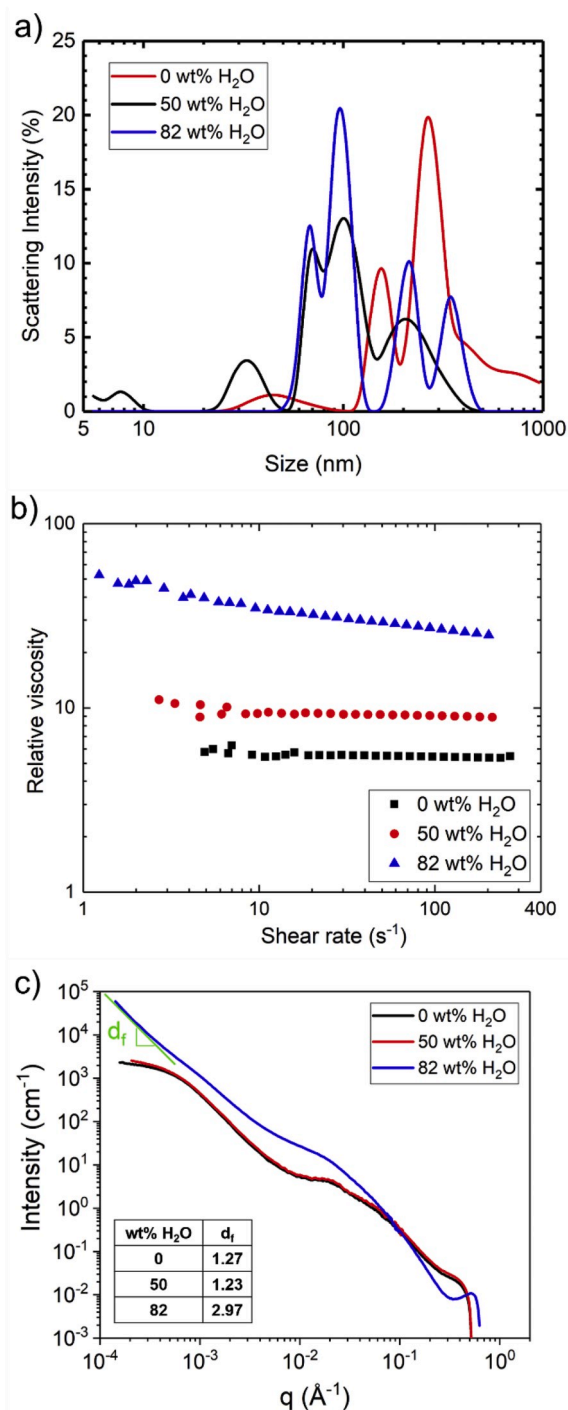


**Fig. 8.** a) DLS measurement of scattering intensity by size distribution plots of 0.024 wt% ionomer dispersion in different H<sub>2</sub>O-nPA wt% solutions. b) Steady-shear relative viscosity data of catalyst inks with 35 wt% ionomer and different wt% H<sub>2</sub>O contents. c) USAXS scattering curves of catalyst inks with different wt % H<sub>2</sub>O contents. Tabulated values of the mass fractal dimension  $d_f$  from  $I(q) \sim q^{-d_f}$  power-law fit to low- $q$  data below 0.001 from Guinier fit to the data are also shown.

#### 4. Conclusions

In this work, the performance of three different PGM-free CCLs fabricated with the same catalyst loading and ionomer content, but different ink composition in terms of nPA and H<sub>2</sub>O content was investigated. Overall, up to a 50% performance improvement was observed in

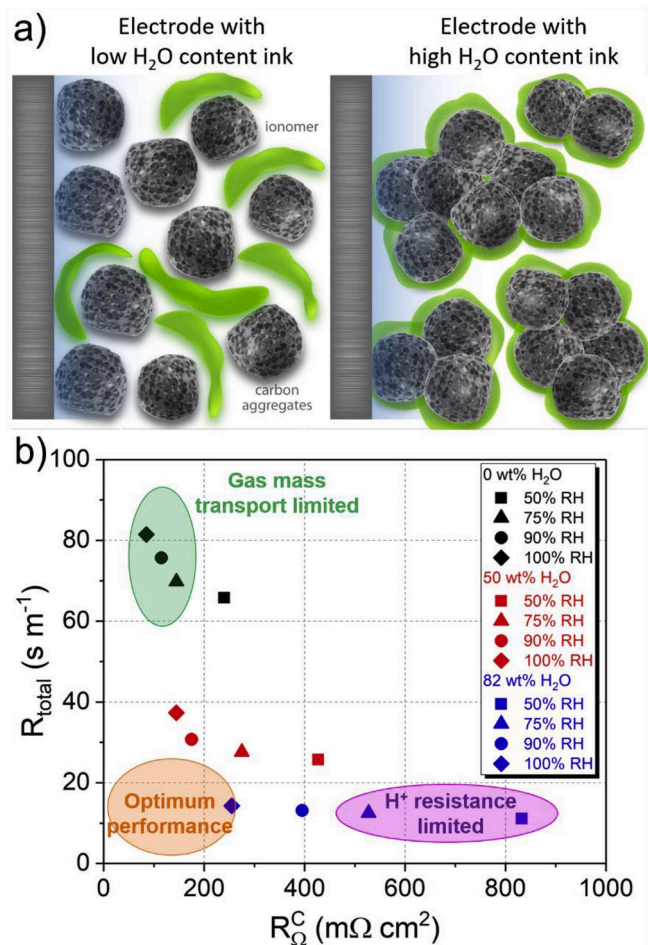


**Fig. 9.** a) Scheme representing the impact of H<sub>2</sub>O content in the ink on the electrode structure for the Fe-N-C catalyst used in this study. b) Gas-phase bulk mass transport resistance in function of proton resistance in the CCL measured at different RH for the electrodes fabricated with different H<sub>2</sub>O contents in the ink solvent.

H<sub>2</sub>/air polarization measurements at 100% RH for an electrode prepared with 82 wt% H<sub>2</sub>O in the ink, compared to the case with only nPA.

All electrodes were characterized for gas-phase mass transport resistance, electrode capacitance, and proton resistance as a function of cell RH. In addition, electrode structure and ionomer distribution were investigated using STEM-EDS and nano-CT. In doing so, we demonstrated that the aggregation and interactions dictated by tuning the ink formulation modifies the electrode properties and in turn the PEFC performance. It was determined that a water-rich ink formulation helps to obtain better gas-phase mass transport properties, increasing the H<sub>2</sub>/air PEFC performance at high RH, where the mass transport within the CCL pores is more arduous due to presence of liquid water and the effect of ionomer swelling. Conversely, a 50/50 wt% mixture of H<sub>2</sub>O and nPA resulted in a maximum adsorption of ionomer on the electrocatalyst surface, increasing electrode capacitance at lower RH, improving robustness and maximizing performance at 75% RH. Lastly, inks comprised of entirely nPA limit adsorption of ionomer on electrocatalyst. This limited interaction results in ionomer located in the pores of the electrode and while beneficial for proton transport, manifests as the highest gas transport resistances of any of the electrode studied here.

While we are fully aware that interactions may change as ionomer chemistry and electrocatalyst properties are altered, these results demonstrate that electrode optimization and novel electrode designs that improve proton conductivity and bulk-electrode gas transport are critical for the improvement of PGM-free electrodes performance as

much as the increases in catalyst activity and stability.

## Declaration of competing interest

None.

## CRediT authorship contribution statement

**Luigi Osmieri:** Writing - original draft, Conceptualization, Methodology, Investigation, Formal analysis, Visualization. **Guanxiong Wang:** Conceptualization, Methodology, Investigation, Validation, Formal analysis, Visualization. **Firat C. Cetinbas:** Investigation, Formal analysis, Visualization. **Sunilkumar Khandavalli:** Investigation, Formal analysis, Visualization. **Jaehyung Park:** Investigation, Formal analysis. **Samantha Medina:** Investigation, Formal analysis. **Scott A. Mauger:** Supervision, Writing - review & editing. **Michael Ulsh:** Supervision, Project administration, Funding acquisition. **Svitlana Pylypenko:** Supervision, Formal analysis, Writing - review & editing. **Deborah J. Myers:** Supervision, Project administration, Funding acquisition, Formal analysis. **K.C. Neyerlin:** Conceptualization, Writing - review & editing, Supervision, Project administration, Funding acquisition, Formal analysis.

## Acknowledgments

This work was authored in part by Alliance for Sustainable Energy, LLC, the manager and operator of the National Renewable Energy Laboratory for the U.S. Department of Energy under Contract No. DE-AC36-08GO28308. Argonne National Laboratory is managed for the U.S. Department of Energy by the University of Chicago Argonne, LLC, also under contract DE-AC-02-06CH11357. Research performed as part of the Electrocatalysis Consortium (ElectroCat), established as part of the Energy Materials Network, which is supported by the U.S. Department of Energy, Office of Energy Efficiency and Renewable Energy, Fuel Cell Technologies Office. The X-ray tomography experiments were performed at beamline 32-ID-C and the X-ray scattering experiments at beamline 9-ID-C at the Advanced Photon Source at Argonne National Laboratory. Use of the Advanced Photon Source, an Office of Science user facility operated by Argonne National Laboratory, is supported by the U.S. Department of Energy, Office of Science, Office of Basic Energy Sciences, under Contract No. DE-AS02-06CH11357. The authors would like to thank Jan Ilavsky, Ivan Kuzmenko, and Vincent De Andrade of the Advanced Photon Source.

The authors wish to thank Dimitrios Papageorgopoulos and Simon Thompson in FCTO at DOE for supporting this work. While we do not endorse any materials presented in this study, we wish to thank Alexey Serov and Bar Zulevi of Pajarito Powders LLC for the use of their electrocatalysts. The views expressed in the article do not necessarily represent the views of the DOE or the U.S. Government.

## Appendix A. Supplementary data

Supplementary data to this article can be found online at <https://doi.org/10.1016/j.nanoen.2020.104943>.

## References

- [1] M. da Graça Carvalho, M. Bonifacio, P. Dechamps, Building a low carbon society, *Energy* 36 (2011) 1842–1847, <https://doi.org/10.1016/j.energy.2010.09.030>.
- [2] P. Poizot, F. Dolhem, Clean energy new deal for a sustainable world: from non-CO<sub>2</sub> generating energy sources to greener electrochemical storage devices, *Energy Environ. Sci.* 4 (2011) 2003–2019, <https://doi.org/10.1039/c0ee00731e>.
- [3] DOE Fuel Cell Technologies Office, H<sub>2</sub>@Scale - enabling affordable, reliable, clean, and secure energy across sectors (n.d.), <https://www.energy.gov/eere/fuelcells/h2scale>. (Accessed 19 April 2019).
- [4] C. Lemke, F. Grueger, O. Arnold, MELY: market model for water electrolysis – electrolysis' economic potential given its technological feasibility, *Energy Procedia* 73 (2015) 59–68, <https://doi.org/10.1016/j.egypro.2015.07.562>.
- [5] Y. Ligen, H. Vrubel, H. Girault, Mobility from renewable electricity: infrastructure comparison for battery and hydrogen fuel cell vehicles, *World Electr. Veh. J.* 9 (2018) 3, <https://doi.org/10.3390/wevj9010003>.
- [6] A. Coralli, B.J.M. Sarraf, P.E.V. de Miranda, L. Osmieri, S. Specchia, N.Q. Minh, Fuel cells, in: P.E.V. de Miranda (Ed.), *Sci. Eng. Hydrog. Energy Technol.*, Elsevier, 2018, <https://doi.org/10.1016/B978-0-12-814251-6.00002-2>.
- [7] J. Durst, C. Simon, F. Hasche, H.A. Gasteiger, Hydrogen oxidation and evolution reaction kinetics on carbon supported Pt, Ir, Rh, and Pd electrocatalysts in acidic media, *J. Electrochem. Soc.* 162 (2015) F190–F203, <https://doi.org/10.1149/2.0981501jes>.
- [8] Y. Feng, N. Alonso-Vante, Nonprecious metal catalysts for the molecular oxygen-reduction reaction, *Phys. Status Solidi* 245 (2008) 1792–1806, <https://doi.org/10.1002/pssb.200879537>.
- [9] (n.d.) Johnson Matthey. <http://www.platinum.matthey.com/prices>. (Accessed 17 July 2019).
- [10] F. Jaouen, E. Proietti, M. Lefèvre, R. Chenitz, J.-P. Dodelet, G. Wu, H.T. Chung, C. M. Johnston, P. Zelenay, Recent advances in non-precious metal catalysis for oxygen-reduction reaction in polymer electrolyte fuel cells, *Energy Environ. Sci.* 4 (2011) 114–130, <https://doi.org/10.1039/c0ee00011f>.
- [11] D. Banham, S. Ye, Current status and future development of catalyst materials and catalyst layers for proton exchange membrane fuel cells: an industrial perspective, *ACS Energy Lett.* 2 (2017) 629–638, <https://doi.org/10.1021/acseenergylett.6b00644>.
- [12] H.A. Gasteiger, S.S. Kocha, B. Sompalli, F.T. Wagner, Activity benchmarks and requirements for Pt, Pt-alloy, and non-Pt oxygen reduction catalysts for PEMFCs, *Appl. Catal. B Environ.* 56 (2005) 9–35, <https://doi.org/10.1016/j.apcatb.2004.06.021>.
- [13] X.X. Wang, V. Prabhakaran, Y. He, Y. Shao, G. Wu, Iron-free cathode catalysts for proton-exchange-membrane fuel cells: cobalt catalysts and the peroxide mitigation approach, *Adv. Mater.* 1805126 (2019) 1805126, <https://doi.org/10.1002/adma.201805126>.
- [14] U. Martinez, S. Komini Babu, E.F. Holby, H.T. Chung, X. Yin, P. Zelenay, Progress in the development of Fe-based PGM-free electrocatalysts for the oxygen reduction reaction, *Adv. Mater.* (2019) 1806545, <https://doi.org/10.1002/adma.201806545>.
- [15] Y. Shao, J.-P. Dodelet, G. Wu, P. Zelenay, PGM-free cathode catalysts for PEM fuel cells: a mini-review on stability challenges, *Adv. Mater.* 1807615 (2019) 1807615, <https://doi.org/10.1002/adma.201807615>.
- [16] L. Osmieri, Transition metal–nitrogen–carbon (M–N–C) catalysts for oxygen reduction reaction. Insights on synthesis and performance in polymer electrolyte fuel cells, *ChemEngineering* 3 (2019), <https://doi.org/10.3390/chemengineering3010016>.
- [17] H.M. Barkholtz, D.-J. Liu, Advancements in rationally designed PGM-free fuel cell catalysts derived from metal–organic frameworks, *Mater. Horizons.* 4 (2017) 20–37, <https://doi.org/10.1039/C6MH00344C>.
- [18] R. Othman, A.L. Dicks, Z. Zhu, Non precious metal catalysts for the PEM fuel cell cathode, *Int. J. Hydrogen Energy* 37 (2012) 357–372, <https://doi.org/10.1016/j.ijhydene.2011.08.095>.
- [19] D. Banham, J.-Y. Choi, T. Kishimoto, S. Ye, Integrating PGM-free catalysts into catalyst layers and proton exchange membrane fuel cell devices, *Adv. Mater.* 1804846 (2019) 1804846, <https://doi.org/10.1002/adma.201804846>.
- [20] S.T. Thompson, D. Papageorgopoulos, Platinum group metal-free catalysts boost cost competitiveness of fuel cell vehicles, *Nat. Catal.* 2 (2019) 558–561, <https://doi.org/10.1038/s41929-019-0291-x>.
- [21] L. Osmieri, R.K. Ahluwalia, X. Wang, H.T. Chung, X. Yin, A.J. Kropf, J. Park, D. A. Cullen, K.L. More, P. Zelenay, D.J. Myers, K.C. Neyerlin, Elucidation of PGM-free electrocatalyst active site functionality via in-situ X-ray absorption and operando determination of oxygen reduction reaction kinetics in a PEFC, *Appl. Catal. B Environ.* 257 (2019) 117929, <https://doi.org/10.1016/j.apcatb.2019.117929>.
- [22] F.C. Cetinbas, R.K. Ahluwalia, Agglomerates in polymer electrolyte fuel cell electrodes: Part II. Transport characterization, *J. Electrochem. Soc.* 165 (2018) F1059–F1066, <https://doi.org/10.1149/2.0301813jes>.
- [23] S. Komini Babu, H.T. Chung, P. Zelenay, S. Litster, Resolving electrode morphology's impact on platinum group metal-free cathode performance using nano-CT of 3D hierarchical pore and ionomer distribution, *ACS Appl. Mater. Interfaces* 8 (2016) 32764–32777, <https://doi.org/10.1021/acsami.6b08844>.
- [24] X. Yin, L. Lin, H.T. Chung, S. Komini Babu, U. Martinez, G.M. Purdy, P. Zelenay, Effects of MEA fabrication and ionomer composition on fuel cell performance of PGM-free ORR catalyst, *ECS Trans* 77 (2017) 1273–1281, <https://doi.org/10.1149/07711.1273ecst>.
- [25] F. Jaouen, D. Jones, N. Coutard, V. Artero, P. Strasser, A. Kucernak, Toward platinum group metal-free catalysts for hydrogen/air proton-exchange membrane fuel cells, *Johnson Matthey Technol. Rev.* 62 (2018) 231–255, <https://doi.org/10.1595/205651318X696828>.
- [26] C.S. Gittleman, A. Kongkanand, D. Masten, W. Gu, Materials research and development focus areas for low cost automotive proton-exchange membrane fuel cells, *Curr. Opin. Electrochem.* 18 (2019) 81–89, <https://doi.org/10.1016/j.coelec.2019.10.009>.
- [27] G. Wang, L. Osmieri, A.G. Star, J.R. Pfeilsticker, K.C. Neyerlin, Elucidating the role of ionomer in the performance of platinum group metal-free catalyst layer via in-situ electrochemical diagnostics, *J. Electrochem. Soc.* 167 (2020), 044519.
- [28] L. Osmieri, S.A. Mauger, M. Ulsh, K.C. Neyerlin, G. Bender, Use of a segmented cell for the combinatorial development of platinum group metal-free electrodes for polymer electrolyte fuel cells, *J. Power Sources* 452 (2020) 227829, <https://doi.org/10.1016/j.jpowsour.2020.227829>.



- [29] L. Osmieri, R. Escudero-Cid, A.H.A. Monteverde Videla, P. Ocón, S. Specchia, Performance of a Fe-N-C catalyst for the oxygen reduction reaction in direct methanol fuel cell: cathode formulation optimization and short-term durability, *Appl. Catal. B Environ.* 201 (2017) 253–265, <https://doi.org/10.1016/j.apcatb.2016.08.043>.
- [30] Y. Garsany, R.W. Atkinson, M.B. Sassin, R.M.E. Hjelm, B.D. Gould, K.E. Swider-Lyons, Improving PEMFC performance using short-side-chain low-equivalent-weight PFSA ionomer in the cathode catalyst layer, *J. Electrochem. Soc.* 165 (2018) F381–F391, <https://doi.org/10.1149/2.1361805jes>.
- [31] T. Van Cleve, S. Khandavalli, A. Chowdhury, S. Medina, S. Pylypenko, M. Wang, K. L. More, N. Kariuki, D.J. Myers, A.Z. Weber, S.A. Mauger, M. Ulsh, K.C. Neyerlin, Dictating Pt-based electrocatalyst performance in polymer electrolyte fuel cells, from formulation to application, *ACS Appl. Mater. Interfaces* 11 (2019) 46953–46964, <https://doi.org/10.1021/acsami.9b17614>.
- [32] K.B. Hatzell, M.B. Dixit, S.A. Berlinger, A.Z. Weber, Understanding inks for porous-electrode formation, *J. Mater. Chem. A* 5 (2017) 20527–20533, <https://doi.org/10.1039/c7ta07255d>.
- [33] A. Orfanidi, P.J. Rheinländer, N. Schulte, H.A. Gasteiger, Ink solvent dependence of the ionomer distribution in the catalyst layer of a PEMFC, *J. Electrochem. Soc.* 165 (2018) F1254–F1263, <https://doi.org/10.1149/2.1251814jes>.
- [34] H.K. Lee, J.H. Park, D.Y. Kim, T.H. Lee, A study on the characteristics of the diffusion layer thickness and porosity of the PEMFC, *J. Power Sources* 131 (2004) 200–206, <https://doi.org/10.1016/j.jpowsour.2003.12.039>.
- [35] S.A. Mauger, K.C. Neyerlin, A.C. Yang-Neyerlin, K.L. More, M. Ulsh, Gravure coating for roll-to-roll manufacturing of proton-exchange-membrane fuel cell catalyst layers, *J. Electrochem. Soc.* 165 (2018) F1012–F1018, <https://doi.org/10.1149/2.0091813jes>.
- [36] J. Liu, M.R. Talarposhti, T. Asset, D.C. Sabarirajan, D.Y. Parkinson, P. Atanassov, I. V. Zenyuk, Understanding the role of interfaces for water management in platinum group metal-free electrodes in polymer electrolyte fuel cells, *ACS Appl. Energy Mater.* 2 (2019) 3542–3553, <https://doi.org/10.1021/acsaelm.9b00292>.
- [37] R.K. Ahluwalia, X. Wang, L. Osmieri, J.-K. Peng, H.T. Chung, K.C. Neyerlin, Activity of atomically dispersed (AD) Fe-C-N ORR catalyst in polymer electrolyte fuel cell environment, *J. Electrochem. Soc.* 166 (2019) F1096–F1104, <https://doi.org/10.1149/2.0851914jes>.
- [38] L. Osmieri, A.H.A. Monteverde Videla, S. Specchia, The use of different types of reduced graphene oxide in the preparation of Fe-N-C electrocatalysts: capacitive behavior and oxygen reduction reaction activity in alkaline medium, *J. Solid State Electrochem.* 20 (2016) 3507–3523, <https://doi.org/10.1007/s10008-016-3332-2>.
- [39] E. Frackowiak, F. Béguin, Carbon materials for the electrochemical storage of energy in capacitors, *Carbon* N. Y. 39 (2001) 937–950, [https://doi.org/10.1016/S0008-6223\(00\)00183-4](https://doi.org/10.1016/S0008-6223(00)00183-4).
- [40] E.B. Easton, P.G. Pickup, An electrochemical impedance spectroscopy study of fuel cell electrodes, *Electrochim. Acta* 50 (2005) 2469–2474, <https://doi.org/10.1016/j.electacta.2004.10.074>.
- [41] G. Li, P.G. Pickup, Ionic conductivity of PEMFC electrodes, *J. Electrochem. Soc.* 150 (2003) C745–C752, <https://doi.org/10.1149/1.1611493>.
- [42] M.C. Lefebvre, R.B. Martin, P.G. Pickup, Characterization of ionic conductivity profiles within proton exchange membrane fuel cell gas diffusion electrodes by impedance spectroscopy, *Electrochem. Solid State Lett.* 2 (1999) 259–261, <https://doi.org/10.1149/1.1390804>.
- [43] R. Makharia, M.F. Mathias, D.R. Baker, Measurement of catalyst layer electrolyte resistance in PEFCs using electrochemical impedance spectroscopy, *J. Electrochem. Soc.* 152 (2005) A970A–A977, <https://doi.org/10.1149/1.1888367>.
- [44] A.G. Star, G. Wang, S. Medina, S. Pylypenko, K.C. Neyerlin, Mass transport characterization of platinum group metal-free polymer electrolyte fuel cell electrodes using a differential cell with an integrated electrochemical sensor, *J. Power Sources* 450 (2020) 227655.
- [45] S.A. Mauger, J.R. Pfeilsticker, M. Wang, S. Medina, A.C. Yang-Neyerlin, K. C. Neyerlin, C. Stetson, S. Pylypenko, M. Ulsh, Fabrication of high-performance gas-diffusion-electrode based membrane-electrode assemblies, *J. Power Sources* 450 (2020) 227581, <https://doi.org/10.1016/j.jpowsour.2019.227581>.
- [46] D.R. Baker, D.A. Caulk, K.C. Neyerlin, M.W. Murphy, Measurement of oxygen transport resistance in PEM fuel cells by limiting current methods, *J. Electrochem. Soc.* 156 (2009) B991–B1003, <https://doi.org/10.1149/1.3152226>.
- [47] S. Kabir, D.J. Myers, N.N. Kariuki, J. Park, G. Wang, N. Macauley, R. Mukundan, K. L. More, K.C. Neyerlin, Elucidating the dynamic nature of fuel cell electrodes as a function of Conditioning : an ex-situ materials characterization and in-situ electrochemical diagnostic study, *ACS Appl. Mater. Interfaces* 11 (2019) 45016–45030, <https://doi.org/10.1021/acsami.9b11365>.
- [48] F.C. Cetinbas, X. Wang, R.K. Ahluwalia, N.N. Kariuki, R.P. Winarski, Z. Yang, J. Sharman, D.J. Myers, Microstructural analysis and transport resistances of low-platinum-loaded PEFC electrodes, *J. Electrochem. Soc.* 164 (2017) F1596–F1607, <https://doi.org/10.1149/2.1111714jes>.
- [49] J. Ilavsky, F. Zhang, A.J. Allen, L.E. Levine, P.R. Jemian, G.G. Long, Ultra-small-angle X-ray scattering instrument at the advanced photon source: history, recent development, and current status, *Metall. Mater. Trans. A Phys. Metall. Mater. Sci.* 44 (2013) 68–76, <https://doi.org/10.1007/s11661-012-1431-y>.
- [50] J. Ilavsky, P.R. Jemian, Irena: tool suite for modeling and analysis of small-angle scattering, *J. Appl. Crystallogr.* 42 (2009) 347–353.
- [51] M. Safollah, P.E.A. Melchy, P. Berg, M. Eikerling, Model of water sorption and swelling in polymer electrolyte membranes: diagnostic applications, *J. Phys. Chem. B* 119 (2015) 8165–8175, <https://doi.org/10.1021/acs.jpcc.5b00486>.
- [52] M.H. Eikerling, P. Berg, Poroelastic theory of water sorption and swelling in polymer electrolyte membranes, *Soft Matter* 7 (2011) 5976–5990, <https://doi.org/10.1039/c1sm05273j>.
- [53] X. Yin, P. Zelenay, Kinetic models for the degradation mechanisms of PGM-free ORR catalysts, *ECS Trans* 85 (2018) 1239–1250.
- [54] J. Christunoff, RRDE and voltammetric study of ORR on pyrolyzed Fe/polyaniline catalyst. On the origins of variable tafel slopes, *J. Phys. Chem. C* 115 (2011) 6496–6507.
- [55] J. Li, A. Alsudairi, Z.-F. Ma, S. Mukerjee, Q. Jia, Asymmetric volcano trend in oxygen reduction activity of Pt and non-Pt catalysts: in situ identification of the site-blocking effect, *J. Am. Chem. Soc.* 139 (2017) 1384–1387, <https://doi.org/10.1021/jacs.6b11072>.
- [56] A.H.A. Monteverde Videla, L. Osmieri, M. Armandi, S. Specchia, Varying the morphology of Fe-N-C electrocatalysts by templating Iron Phthalocyanine precursor with different porous SiO<sub>2</sub> to promote the Oxygen Reduction Reaction, *Electrochim. Acta* 177 (2015) 43–50, <https://doi.org/10.1016/j.electacta.2015.01.165>.
- [57] Q. Jia, N. Ramaswamy, H. Hafiz, U. Tylus, K. Strickland, G. Wu, B. Barbiellini, A. Bansil, E.F. Holby, P. Zelenay, S. Mukerjee, Experimental observation of redox-induced Fe-N switching behavior as a determinant role for oxygen reduction activity, *ACS Nano* 9 (2015) 12496–12505, <https://doi.org/10.1021/acsnano.5b05984>.
- [58] H.T. Chung, D.A. Cullen, D. Higgins, B.T. Sneed, E.F. Holby, K.L. More, P. Zelenay, Direct atomic-level insight into the active sites of a high-performance PGM-free ORR catalyst, *Science* 357 (80) (2017) 479–484, <https://doi.org/10.1126/science.aan2255>.
- [59] J.-Y. Choi, L. Yang, T. Kishimoto, X. Fu, S. Ye, Z. Chen, D. Banham, Is the rapid initial performance loss of Fe/N/C non precious metal catalysts due to micropore flooding? *Energy Environ. Sci.* 10 (2017) 296–305, <https://doi.org/10.1039/C6EE03005J>.
- [60] L. Xing, P.K. Das, X. Song, M. Mamlouk, K. Scott, Numerical analysis of the optimum membrane/ionomer water content of PEMFCs: the interaction of Nafion® ionomer content and cathode relative humidity, *Appl. Energy* 138 (2015) 242–257, <https://doi.org/10.1016/j.apenergy.2014.10.011>.
- [61] V. Yarlaga, M.K. Carpenter, T.E. Moylan, R.S. Kukreja, R. Koestner, W. Gu, L. Thompson, A. Kongkanand, Boosting fuel cell performance with accessible carbon mesopores, *ACS Energy Lett* 3 (2018) 618–621, <https://doi.org/10.1021/acscenergylett.8b00186>.
- [62] J. Song, M.Z. Bazant, Effects of nanoparticle geometry and size distribution on diffusion impedance of battery electrodes, *J. Electrochem. Soc.* 160 (2013) A15–A24, <https://doi.org/10.1149/2.023301jes>.
- [63] M. Obermaier, A.S. Bandarenka, C. Lohri-Tymozhynsky, A comprehensive physical impedance model of polymer electrolyte fuel cell cathodes in oxygen-free atmosphere, *Sci. Rep.* 8 (2018) 1–9, <https://doi.org/10.1038/s41598-018-23071-5>.
- [64] K.C. Neyerlin, W. Gu, J. Jorne, A. Clark, H.A. Gasteiger, Cathode catalyst utilization for the ORR in a PEMFC, *J. Electrochem. Soc.* 154 (2007) B279–B287, <https://doi.org/10.1149/1.2400626>.
- [65] T. Jacobsen, K. West, Diffusion impedance IN planar, cylindrical and spherical symmetry, *Electrochim. Acta* 40 (1995) 255–262, [https://ac.els-cdn.com/0013468694E01923/1-s2.0-0013468694E01923-main.pdf?tid=31c71918-2c2f-4f12-86e5-19be71828e2b&acdnat=1551483789\\_2ef409a8257c0fca604e09c3f6183368](https://ac.els-cdn.com/0013468694E01923/1-s2.0-0013468694E01923-main.pdf?tid=31c71918-2c2f-4f12-86e5-19be71828e2b&acdnat=1551483789_2ef409a8257c0fca604e09c3f6183368).
- [66] J.P. Meyers, M. Doyle, R.M. Darling, J. Newman, The impedance response of a porous electrode composed of intercalation particles, *J. Electrochem. Soc.* 147 (2002) 2930, <https://doi.org/10.1149/1.1393627>.
- [67] M.A. Modestino, D.K. Paul, S. Dishari, S.A. Petrina, F.I. Allen, M.A. Hickner, K. Karan, R.A. Segalman, A.Z. Weber, Self-assembly and transport limitations in confined nafion films, *Macromolecules* 46 (2013) 867–873, <https://doi.org/10.1021/ma301999a>.
- [68] D.K. Paul, K. Karan, Conductivity and wettability changes of ultrathin nafion films subjected to thermal annealing and liquid water exposure, *J. Phys. Chem. C* 118 (2014) 1828–1835, <https://doi.org/10.1021/jp410510x>.
- [69] S.A. Berlinger, B.D. McCloskey, A.Z. Weber, Inherent acidity of perfluorosulfonic acid ionomer dispersions and implications for ink aggregation, *J. Phys. Chem. B* 122 (2018) 7790–7796, <https://doi.org/10.1021/acs.jpcc.8b06493>.
- [70] P.J. Dudenas, A. Kusoglu, Evolution of ionomer morphology from dispersion to film: an in situ X-ray study, *Macromolecules* (2019) 7779–7785, <https://doi.org/10.1021/acs.macromol.9b01024>.
- [71] S. Litster, W.K. Epting, E.A. Wargo, S.R. Kalidindi, E.C. Kumbar, Morphological analyses of polymer electrolyte fuel cell electrodes with nano-scale computed tomography imaging, *Fuel Cell* 13 (2013) 935–945, <https://doi.org/10.1002/fuce.201300008>.
- [72] W.K. Epting, J. Gelb, S. Litster, Resolving the three-dimensional microstructure of polymer electrolyte fuel cell electrodes using nanometer-scale X-ray computed tomography, *Adv. Funct. Mater.* 22 (2012) 555–560, <https://doi.org/10.1002/adfm.201101525>.
- [73] S. Komini Babu, A.I. Mohamed, J.F. Whitacre, S. Litster, Multiple imaging mode X-ray computed tomography for distinguishing active and inactive phases in lithium-ion battery cathodes, *J. Power Sources* 283 (2015) 314–319, <https://doi.org/10.1016/j.jpowsour.2015.02.086>.
- [74] S. Komini Babu, H.T. Chung, G. Wu, P. Zelenay, S. Litster, Modeling hierarchical non-precious metal catalyst cathodes for PEFCs using multi-scale X-ray CT imaging, *ECS Trans* 64 (2014) 281–292, <https://doi.org/10.1149/06403.0281ecst>.
- [75] M. Yamaguchi, T. Matsunaga, K. Amemiya, A. Ohira, N. Hasegawa, K. Shinohara, M. Ando, T. Yoshida, Dispersion of rod-like particles of nafion in salt-free water/1-propanol and water/ethanol solutions, *J. Phys. Chem. B* 118 (2014) 14922–14928, <https://doi.org/10.1021/jp506814m>.
- [76] S. Takahashi, J. Shimanuki, T. Mashio, A. Ohma, H. Tohma, A. Ishihara, Y. Ito, Y. Nishino, A. Miyazawa, Observation of ionomer in catalyst ink of polymer



electrolyte fuel cell using cryogenic transmission electron microscopy, *Electrochim. Acta* 224 (2017) 178–185, <https://doi.org/10.1016/j.electacta.2016.12.068>.

- [77] F.M. Pang, C.E. Seng, T.T. Teng, M.H. Ibrahim, Densities and viscosities of aqueous solutions of 1-propanol and 2-propanol at temperatures from 293.15 K to 333.15 K, *J. Mol. Liq.* 136 (2007) 71–78, <https://doi.org/10.1016/j.molliq.2007.01.003>.
- [78] J. Chlistunoff, J.-M. Sansiñena, On the use of Nafion® in electrochemical studies of carbon supported oxygen reduction catalysts in aqueous media, *J. Electroanal. Chem.* 780 (2016) 134–146, <https://doi.org/10.1016/j.jelechem.2016.09.014>.
- [79] S. Khandavalli, J.H. Park, N.N. Kariuki, D.J. Myers, J.J. Stickel, K. Hurst, K. C. Neyerlin, M. Ulsh, S.A. Mauger, Rheological investigation on the microstructure of fuel cell catalyst inks, *ACS Appl. Mater. Interfaces* 10 (2018) 43610–43622, <https://doi.org/10.1021/acsami.8b15039>.
- [80] R.N. Andrews, J. Serio, G. Muralidharan, J. Ilavsky, An in situ USAXS-SAXS-WAXS study of precipitate size distribution evolution in a model Ni-based alloy, *J. Appl. Crystallogr.* 50 (2017) 734–740, <https://doi.org/10.1107/S1600576717006446>.
- [81] G. Beaucage, Small-angle scattering from polymeric mass fractals of arbitrary mass-fractal dimension, *J. Appl. Crystallogr.* 29 (1996) 134–146.
- [82] S. Litster, G. McLean, PEM fuel cell electrodes, *J. Power Sources* 130 (2004) 61–76, <https://doi.org/10.1016/j.jpowsour.2003.12.055>.
- [83] E.L. Thompson, D. Baker, Proton conduction on ionomer-free Pt surfaces, *ECS Trans* 41 (2011) 709–720, <https://doi.org/10.1149/1.3635605>.
- [84] E. Passalacqua, F. Lufrano, G. Squadrito, a Patti, L. Giorgi, Nafion content in the catalyst layer of polymer electrolyte fuel cells: effects on structure and performance, *Electrochim. Acta* 46 (2001) 799–805, [https://doi.org/10.1016/S0013-4686\(00\)00679-4](https://doi.org/10.1016/S0013-4686(00)00679-4).
- [85] J. Liu, I.V. Zenyuk, Proton transport in ionomer-free regions of polymer electrolyte fuel cells and implications for oxygen reduction reaction, *Curr. Opin. Electrochem.* 12 (2018) 202–208, <https://doi.org/10.1016/j.coelec.2018.11.015>.



**Firat C. Cetinbas** earned his Ph.D. in mechanical engineering from University of Delaware, USA in 2014. After graduating, he started working in the Nuclear Engineering division at Argonne National Laboratory, USA (ANL) as a postdoctoral researcher. Currently, he is a mechanical engineer in the Energy System division at ANL. His research focuses on advanced computational techniques, data analysis and microstructure characterization using X-ray tomography.



**Sunilkumar Khandavalli** received his Ph.D. in Mechanical Engineering in 2017 from University of Massachusetts Amherst, USA. He is currently a postdoctoral researcher in Chemistry and Nanoscience Center at National Renewable Energy Laboratory, USA. His research primarily focuses on microstructure and rheology of catalyst inks for fuel cell and electrolyzer technologies.



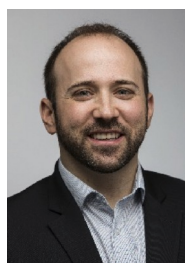
**Luigi Osmieri** obtained his Ph.D. in Chemical Engineering in 2016 from the Politecnico di Torino, Italy. Then he worked as postdoctoral researcher at the Universidad Autónoma de Madrid, Spain. Currently he is a postdoctoral researcher in the Chemistry and Nanoscience Center at the National Renewable Energy Laboratory, USA. His main research interests are PGM-free catalysts for oxygen reduction reaction, electrocatalysis, electrochemical reactions kinetics, and polymer electrolyte fuel cell electrodes development and testing. He is the author of 25 publications between peer-reviewed papers and book chapters.



**Scott A. Mauger** obtained his Ph.D. in Chemical Engineering in 2013 from the University of California, Davis. He is a Scientist in the Chemistry and Nanoscience Center at the National Renewable Energy Laboratory. His research activities focus on the process science and engineering of manufacturing for electrochemical energy conversion technologies and includes research to understand interparticle interactions in catalyst inks and the influence of coating methodologies on catalyst layer properties and performance.



**Guanxiong Wang** obtained his Ph.D. in Chemical Engineering in 2016 from Illinois Institute of Technology, USA. He is now a postdoctoral researcher working in the Chemistry and Nanoscience Division, at the National Renewable Energy Laboratory, USA. His main research interests are PGM and PGM-free catalysts development for oxygen reduction reaction, electrochemical reactions kinetics, and electrochemical energy conversion. He is also expertized on the novel electrode structure design and polymer electrolyte fuel cell electrodes test and characterization. He is the author of more than 20 publications between peer-reviewed papers and book chapters.



**Kenneth C. Neyerlin** obtained his Ph.D. in Chemical Engineering in 2007 from the University of Rochester. He is a Senior Scientist in the Chemistry and Nanoscience Center in the Electrochemical Engineering & Materials Chemistry Group at the National Renewable Energy Laboratory. His research activities focus on the integration of materials for functional electrodes in electrochemical energy conversion technologies as well as the development and application of in-situ electrochemical diagnostics to elucidate the voltage loss contributions of fundamental processes.